

# MODELS OF LOW MASS STARS

A Thesis  
Submitted to the Faculty  
in partial fulfillment of the requirements for the  
degree of

Doctor of Philosophy

in  
Physics and Astronomy  
by Emily M. Boudreaux

Guarini School of Graduate and Advances Studies  
Dartmouth College  
Hanover, New Hampshire

April 2024

Examining Committee:

---

(chair) ***Brian C. Chaboyer***

---

***Elisabeth R. Newton***

---

***Aaron Dotter***

---

***Jamie Tayar***

---

F. Jon Kull, Ph.D.  
Dean of the Guarini School of Graduate and Advanced Studies

### **Copyright Notice**

This work is licensed under the Creative Commons  
Attribution-NonCommercial-ShareAlike 4.0 International License.

To view a copy of this license, visit

<http://creativecommons.org/licenses/by-nc-sa/4.0/>

or send a letter to

Creative Commons, PO Box 1866, Mountain View, CA 94042, USA.

*For Poppy, who taught me to build and supported as I did.*

## Abstract

Low mass stars account for approximately 70 percent of the stellar populations; yet, due to their small sizes and cool temperatures they account for only **NUMBER** percent of the galaxies luminosity function. Consequently, across multiple domains there has been a dearth of interest in these key astronomical objects. In this thesis I present two projects which have further revealed properties of low mass stars. Firstly, I present chemically self consistent models of the globular clusters NGC 2808 and NGC 6752. Due to the ages of both clusters, these models are dominated by low mass stars. We find that chemical consistency between a stars structural and atmospheric models makes only a trivial difference in model predictions. Secondly, I present a detailed investigation into the Gaia M Dwarf Gap (the Jao Gap) looking at how the Jao Gap's theoretical location is effected by high temperature radiative opacity source and how the physics which drives the Jao Gap's formation may also drive perturbations to stellar magnetic field strength.

## Preface

This work was conducted under the supervision of Brian Chaboyer and I would not have been able to complete this thesis without his continued support. I would like to thank Brian immensely for his continued support and for being a wonderful teacher. Further, I am more grateful than words can express for the love and support which my parents, Karol and Don, have provided me throughout my entire life. They have guided, cared, and loved me from the day I told them I was going to be an astronomer in pre-school to the day I defend this thesis. Finally, I would like to thank my friends for always being there for me and for making graduate school both fun and an incredible learning experience.

# Contents

<b>I</b>	<b>Introduction</b>	<b>1</b>
<b>1</b>	<b>A Breif History of Humans &amp; Stars</b>	<b>3</b>
1.1	A post prelude prelude . . . . .	3
1.2	Stars In Ancient Times . . . . .	4
1.3	Astronomy Becomes a Science . . . . .	4
1.4	The Birth of Modern Astronomy . . . . .	5
<b>2</b>	<b>Stars in the Modern World</b>	<b>7</b>
<b>3</b>	<b>Stellar Structure Evolution</b>	<b>9</b>
<b>4</b>	<b>Stars as Stellar Laboratories</b>	<b>11</b>
<b>II</b>	<b>Globular Clusters</b>	<b>13</b>
<b>5</b>	<b>Why Study Globular Clusters</b>	<b>15</b>
<b>6</b>	<b>Modeling Globular Clusters</b>	<b>17</b>
6.1	Problems Modeling Globular Clusters . . . . .	17
<b>7</b>	<b>Modeling NGC 2808</b>	<b>19</b>
7.1	Introduction . . . . .	19
7.2	Stellar Models . . . . .	22
7.3	Chemical Consistency . . . . .	24
7.3.1	Atmospheric Boundary Conditions . . . . .	24

7.3.2	Opacities	25
7.4	fidanka	26
7.4.1	Fiducial Line Measurement	26
7.4.2	Stellar Population Synthesis	32
7.4.3	Isochrone Optimization	32
7.4.4	Fidanka Testing	33
7.5	Isochrone Fitting	34
7.5.1	The Number of Populartions in NGC 2808	36
7.5.2	ACS-HUGS Photometric Zero Point Offset	36
7.6	Results	38
7.6.1	The Number of Populartions in NGC 2808	39
7.7	Conclusion	39
<b>8</b>	<b>Modeling NGC 6752</b>	<b>41</b>
<b>III</b>	<b>Magnetic Fields and the Gaia M dwarf Gap</b>	<b>43</b>
<b>9</b>	<b>Magnetic Fields In M Dwarfs</b>	<b>45</b>
9.1	Magnetic Activity in M dwarfs	45
9.2	Observations & Data Reduction	48
9.3	Analysis	49
9.3.1	Rotation and Rossby Number	52
9.4	Rotation–Activity Relation	53
9.5	Magnetic Activities in M dwarfs Closing Thoughts	60
<b>10</b>	<b>Gap Sensitivity to Opacity Source</b>	<b>61</b>
10.1	INTRODUCTION	61
10.2	Jao Gap	63
10.2.1	Efforts to Model the Gap	64
10.3	Updated Opacities	66
10.3.1	Table Querying and Conversion	67

10.3.2 Solar Calibrated Stellar Models . . . . .	68
10.4 pyTOPSScrape . . . . .	69
10.5 Interpolating $\rho \rightarrow R$ . . . . .	70
10.6 Modeling . . . . .	71
10.6.1 Population Synthesis . . . . .	72
10.6.2 Mixing Length Dependence . . . . .	75
10.7 Results . . . . .	77
<b>11 Jao Gap connection to Magnatism</b>	<b>81</b>
11.1 INTRODUCTION . . . . .	81
11.2 Correlation . . . . .	83
11.2.1 Rotation . . . . .	87
11.2.2 Limitations . . . . .	89
11.3 Modeling . . . . .	89
11.3.1 Limitations . . . . .	92
11.4 Conclusion . . . . .	93
<b>IV Conclusions</b>	<b>95</b>



# List of Tables

7.1	Relative Metal composition used where $a(H) = 12$ . Where the relative composition is the same for both populations A and E it is only listed in the population A column for the sake of visual clarity. . . . .	23
7.2	Best fit parameters derived from fitting isochrones to the fiducial lines derived from the NCG 2808 photometry. . . . .	35
7.3	Best fit parameters derived from fitting isochrones to the fiducial lines derived from the NCG 2808 photometry. . . . .	39
9.1	Calculated Rossby Numbers and $R'_{HK}$ values. All circular data points in Figures 9.2 & 9.3 are present in this table. Masses are taken from the MEarth database. A machine readable version of this table is <b>available</b>	55
10.1	Optimized parameters for SCSMs evolved using OPAL and OPLIB high temperature opacity tables. . . . .	69
10.2	Locations identified as potential Gaps. . . . .	78



# List of Figures

7.1	Comparison of the MARCS model atmospheres generated for the two extreme populations of NGC 2808. These lines shows population A and E with the same Helium abundance; though, we fit a grid of models over various helumn abundances. Dashed lines show the temperature of the boundary condition while sold lines show the pressure. . . . .	25
7.2	Density map demo showing density estimate over different parts of the evolutionary sequence. The left panel shows the density map over the entire evolutionary sequence, while the middle panel shows the density map over the main sequence and the right most panel shows the density map over the RGB. Figures in the top row are the raw CMD, while figures in the bottom row are colored by the density map. . . . .	28
7.3	CMD where points are colored by density. Lines show the density-color profile in each magnitude bin. In this figure adaptive binning targeted 1000 stars per bin . . . . .	29
7.4	Example of BGMM fit to a magnitude bin. The grey line shows the underlying color-density profile, while the black dashed-line shows the joint distribution of each BGMM component. The solid black lines show the two selected components. . . . .	30
7.5	CMD where points are colored by density. Line trace the infered fiducial line(s) in each magnitude bin. . . . .	31

7.6 Synthetic population generated by fidanka at 10000pc with E(B-V) = 0, and an age of 12 Gyr along with the best fitting isochrone. The best fit paremeters are derived to be $mu = 15.13$ , E(B-V)=0.001, and an age of 12.33 Gyr. . . . .	33
7.7 Percent Error distribution for each of the three deriver parameters. Note that these values will be sensitive to the magnitude uncertainties of the photometry. Here we made use of the ACS artificial star tests to estimate the uncertainties. <a href="#">Note that currently this is built with 100 runs, these take a long time so currently re running with 1000 runs.</a> . . . . .	34
7.8 Best fit isochrone results for NGC 2808. . . . .	35
7.9 Silhouette analysis for NGC 2808 F275W-F814W photometry. The Silhouette scores are an average of score for each magnitude bin. Positive scores incidate that the clustering algorithm produced well distinguished clusters while negative scores indicate clusters which are not well distinguished. . . . .	36
7.10 (left) CMD showing the photometric offset between the ACS and HUGS data for NGC 2808. CMDs have been randomly subsampled and colored by point density for clarity. (right) Mean difference between the color of the HUGS and ACS fiducial lines at the same magnitude. Note that the ACS data is systematically bluer than the HUGS data. . . . .	37
7.11 Main sequence turn off magnitude offset from a guage helium mass fraction (Y=0.30 chosen). All main sequence turn off locations are measured at 12.3 Gyr <a href="#">Should I make these contour surfaces for various ages?</a> . . . . .	38
7.12 Best fit isochrone results for NGC 2808. . . . .	38
9.1 Spectrum of 2MASS J06105288-4324178 overplotted with the S index bandpasses. (top) V band and Ca II K emission line. (bottom) Ca II H emission line and R band. Note that the rectangular and triangular regions denote both the wavelength range of the band and the relative weight assigned to each wavelength in the band while integrating. . . . .	50

9.2 Rotation activity relation from this work. The color axis gives each stars mass. The dashed line is the best fit to our data set. . . . .	54
9.3 Rotation activity relation for both our work and <a href="#">Astudillo-Defru et al. (2017)</a> . The dotted line is the best fit to the re-derived rotation-activity relation from <a href="#">Astudillo-Defru et al. (2017)</a> . Note that targets from <a href="#">Astudillo-Defru et al. (2017)</a> are systematically higher than targets presented here as a consequence of the range in mass probed by the samples. . . . .	56
9.4 Derived rotation-activity curves from this work, <a href="#">Astudillo-Defru et al. (2017)</a> and <a href="#">Mamajek &amp; Hillenbrand (2008)</a> . Note both that <a href="#">Mamajek &amp; Hillenbrand (2008)</a> focuses their work on earlier spectral classes and fits the rotation activity relation in linear space. . . . .	56
9.5 Distribution of masses between our sample and the sample presented in <a href="#">Astudillo-Defru et al. (2017)</a> . Note how the two studies have approximately the same sample sizes; however, our sample is more tightly concentrated at lower masses \later spectral classes. . . . .	60
10.1 The Jao Gap (circled) seen in the Gaia Catalogue of Nearby Stars ( <a href="#">Gaia Collaboration et al., 2021</a> ). . . . .	64
10.2 Diagram for a characteristic stellar model of $0.35625 M_{\odot}$ which is within the Jao Gap's mass range. The black shaded regions denote whether, at a particular model age, a radial shell within the model is radiative (with white meaning convective). The lines trace the models core temperature, core ${}^3\text{He}$ mass fraction, fractional luminosity wrt. the zero age main sequence and fractional radius wrt. the zero age main sequence. . . . .	65

10.3 Rosseland mean opacity with the GS98 solar composition for both OPAL opacities and OPLIB opacities (top). Residuals between OPLIB opacities and OPAL opacities (bottom). These opacities are plotted at $\log_{10}(R) = -0.5$ , $X = 0.7$ , and $Z = 0.02$ . $\log_{10}(R) = -0.5$ approximates much of the interior a $0.35 M_\odot$ model. Note how the OPLIB opacities are systematically lower than the OPAL opacities for temperatures above $10^{5.2}$ K. . . . .	67
10.4 HR Diagram for the two SCSMs, OPAL and OPLIB. OPLIB is shown as a red dashed line. . . . .	68
10.5 Log Fractional Difference between opacities in $\kappa_R(\rho, T_{eff})$ space directly queried from the OPLIB web-form and those which have been interpolated into $\log(R)$ space and back. Note that, due to the temperature grid of type 1 OPAL tables not aligning perfectly with the temperature grid OPLIB uses there may be edge effects where the interpolation is poorly constrained. The red line corresponds to $\log(R) = -0.79$ where much of a stellar model's radius exists. . . . .	71
10.6 Mass-luminosity relation at 7 Gyrs for models evolved using OPAL opacity tables (top) and those evolved using OPLIB opacity tables (bottom). Note the lower mass range of the OPLIB Gap. . . . .	73
10.7 Probability distribution sampled when assigning true parallaxes to synthetic stars. This distribution is built from the GCNS and includes all stars with BP-RP colors between 2.3 and 2.9, the same color range of the Jao Gap. . . . .	74
10.8 Population synthesis results for models evolved with OPAL (left) and models evolved with OPLIB (right). A Gaussian kernel-density estimate has been overlaid to better highlight the density variations. . . . .	75
10.9 CMD showing OPLIB populations (from left to right) A, B, and C. . . . .	76
10.10 Location of the two identified paucities of stars in OPLIB synthetic populations as a function of the mixing length used. . . . .	76

10.11(right panels) OPAL (left) and OPLIB (right) synthetic populations. (left panels) Normalized linear number density along the magnitude axis. A dashed line has been extended from the peak through both panels to make clear where the identified Jao Gap location is wrt. to the population. . . . .	77
10.12Portions of $0.3526 M_{\odot}$ OPAL and OPLIB stellar models showing the interior shells which are radiative (black region). Note that for clarity only one convective mixing event from each model is shown. Note how the radiative zone in the OPLIB model is larger. . . . .	79
10.13Core $^3\text{He}$ mass fraction for $0.3526 M_{\odot}$ models evolved with OPAL and OPLIB (within the Jao Gap's mass range for both). Note how the OPLIB model's core $^3\text{He}$ mass fraction grows at approximately the same rate as the OPAL model's but continues uninterrupted for longer.	80
11.1 Merged Dataset from <a href="#">Boudreault et al. (2022)</a> ; <a href="#">Perdelwitz et al. (2021)</a> . Note the increase in the spread of $R'_{HK}$ around the Jao Gap Magnitude.	84
11.2 Standard deviation of Calcium emission data within each bin. Note the discontinuity near the Jao Gap Magnitude. . . . .	85
11.3 Probability distribution of the false alarm probability for the discontinuity seen in Figure 11.2. The mean of this distribution is $0.341\% \pm^{0.08}_{0.08}$ .	85
11.4 Spread in the magnetic activity metric for the merged sample with any stars $\log(R'_{HK}) > -4.436$ filtered out. . . . .	86
11.5 Probability density distribution of discontinuity location as identified in the merged dataset. The dashed line represents the mean of the distribution while the shaded region runs from the 16th percentile to the 84th percentile of the distribution. This distribution was built from 10,000 independent samples where the discontinuity was identified as the highest value in the gradient of the standard deviation. . . . .	88
11.6 Kippenhan-Iben diagram for a 0.345 solar mass star. Note the periodic mixing events (where the plotted curves peak). . . . .	91

11.7 Example of the toy model presented here resulting in increased divergence between stars magnetic fields. The shaded region represents the maximum spread in the two point correlation function at each age. . . . .	91
11.8 Toy model results showing a qualitatively similar discontinuity in the star-to-star magnetic activity variability. . . . . . . . . . . . .	92

## **Part I**

# **Introduction**



# Chapter 1

## A Breif History of Humans & Stars

*Doubt thou the stars are fire; Doubt that the sun doth move; Doubt the truth  
to be a liar;*

– Hamlet, Act 2, Scene 2

### 1.1 A post prelude prelude

I will start by saying that I am not trained in history and perhaps it is self-indulgent to being with such an amuture overview of another academic field. However, all of the abstraction which we surruond ourselves with in so many of the physical sciences may sometimes sever us from underlying motivations as to why we are interested. It is true that we often speak to the public and to funding agencies about grand ambition and infinite possibility; however, our day-to-day lives are not defined by these things. We spend so much of our time either immersed in the fine details or prostelatizing about greater purpose that I find that I often feel disconected from the real reason I am interested in astronomy. I study astronomy because I am interested in space, there is no greater reason, nothing more substantial than a five year old sitting with their father outside their preschool asking about why the stars and moon are the way that they are. With that being said, please bear with me as I walk us through a breif history of some of the places stars have had in human civilization and the evolution of our understanding of them.

## 1.2 Stars In Ancient Times

The ansestors of humans have no doubt been looking at the sky since before they were humans; however, there are limited ways to study these prehistoric astronomers. Some reminatnts of ealy human (pre-history,  $\gtrapprox$  5000 yrs ago) stargazing to remain, largely in the form of earthn works [CITATION HERE]. The earliest records we have show stars playing an imporant role in religius practices, navigation, and time keeping [CITATION HERE]. These early understandings recognized differences between the fixed stars and the wandering stars though it would be many more centuries and millenia before the full extent of those differences became clear [CITATION HERE].

As far back as the 1300s B.C.E there were accurate star charts being produced by ancient Egyptian, Babylonian, and Chinese astronomers. Fourth century B.C.E Greeks develope star catalougs and many of the moden day English names of stars still derive from these early catalougs.

The understanding of fixed stars at this time was not one of objects similar to our sun; rather, they were thought to be seperate things altogether. Various cosmologies supposed that stars were points on a celestial sphere which surrounded the earth, such as the Babylonian cosmology with posited that the stars existed in a heaven of their own which was interlocked with 2 other heavens.

## 1.3 Astronomy Becomes a Science

The ancient Greeks, Babylonians, and Chinese contributed greatly to our understanding of the universe; however, it was later work, largely by Islamic and Indian scholars which form the basis of what we think of as modern astronomy. These astronomers were not yet conceptualizing the universe the way that we model it today; however, they began systamatzied observations of the universe in ways which would be recognizable. One of the main driving forces of astronomy during this period was nagivation and to that end new instrumentation was developed and early observatories were built. In 934 C.E. *The Book of Fixed Stars* was written by Abd al-Rahman al-Sufi. A expansion of the kinds of catalougs which began over a millenia earlier and

allowed for more precise navigation of ships.

By the 10th Century C.E. Islamic scholars had found evidence that the Earth was not, contrary to Ptolomeic ideas, stationary. In the following centuries multiple criticisms of Ptolemeic theories were published, though none going quite as far as doubting the geocentric model of the universe. One primary change to these ancient theories was the recognition that the Earth rotates about its axis as opposed to the heavens rotating around earth [CITATION HERE].

## 1.4 The Birth of Modern Astronomy

Modern Astronomy does not have a single birth, and different cultures at different points in time have contributed in various ways to our modern understanding.



## Chapter 2

# Stars in the Modern World

Over the last half of the 19th and first decade of the 20th centuries Lane, Ritter, and Emden codified the earliest mathematical model of stellar structure, the polytrope (Equation 2.1), in *Gaskugeln* (Gas Balls) ([Emden, 1907](#)).

$$\frac{d}{d\xi} \left( \xi^2 \frac{d\theta}{d\xi} \right) = -\xi^2 \theta^n \quad (2.1)$$

Where  $\xi$  and  $\theta$  are dimensionless parameterizations of radius and temperature respectively, and  $n$  is known as the polytropic index. Despite this early work, it wasn't until the late 1930s and early 1940s that the full set of equations needed to describe the structure of a steady state, radially-symmetric, star (known as the equations of stellar structure) began to take shape as proton-proton chains and the Carbon-Nitrogen-Oxygen cycle were, for the first time, seriously considered as energy generation mechanisms ([Cowling, 1966](#)). Since then, and especially with the proliferation of computers in astronomy, the equations of stellar structure have proven themselves an incredibly predictive set of models.



## Chapter 3

# Stellar Structure Evolution

There are currently many stellar structure codes (e.g. [Dotter et al., 2008](#); [Kovetz et al., 2009](#); [Paxton et al., 2011](#)) which integrate the equations of stellar structure — in addition to equations of state and lattices of nuclear reaction rates — over time to track the evolution of an individual star. The Dartmouth Stellar Evolution Program (DSEP) ([Chaboyer et al., 2001](#); [Bjork & Chaboyer, 2006](#); [Dotter et al., 2008](#)) is one such, well tested, stellar evolution program.

DSEP solves the equations of stellar structure using the Henyey method ([Henyey et al., 1964](#)). This is a relaxation technique making use of a Newton–Raphson root finder and therefore requires some initial guess to relax towards a solution. This guess will be either some initial, polytropic, model or the solution from the previous timestep. In order to evolve a model through time DSEP alternates between solving for reaction rates and the structure equations. At some temperature and pressure from the solution to the structure equations DSEP finds the energy generation rate due to proton-proton chains, the CNO cycle, and the triple-alpha process from known nuclear cross sections. These reaction rates yield both photon and neutrino luminosities as well as chemical changes over some small time step. Thermodynamic variables are calculated using an equation of state routine which is dependent on the initial model mass. All the updated physical quantities (pressure, luminosity, mean molecular mass, temperature) are then used to solve the structure equations again. This process of using a solution to the structure equations to calculate reaction rates which then

inform the next structure solution continues until DSEP can no longer find a solution. This can happen as the stellar structure equations are extremely stiff. In addition, for finite radial mesh sizes, discontinuities can occur.

While other stellar evolution programs, such as the widely used Modules for Experimentation in Stellar Astrophysics (MESA) ([Paxton et al., 2011](#)), consider a more complex handling of nuclear reaction rate calculations, and are consequently more applicable to a wider range of spectral classes than DSEP, DSEP has certain advantages over these other programs that make it well suited for certain tasks, such as low-mass modeling. For one, DSEP generally can evolve models much more rapidly than MESA and has a smaller memory footprint while doing it. This execution time difference is largely due to the fact that DSEP makes some simplifying assumptions due to its focus only on models with initial masses between  $0.1$  and  $5$   $M_{\odot}$  compared to MESA's more general approach. Moreover, MESA elects to take a very careful handling of numeric uncertainty, going so far as to guarantee byte-to-byte similarity of the same model run on different architectures ([Paxton et al., 2011](#)). DSEP on the other hand makes no such guarantee. Rather, models evolved using DSEP will be accurate down to some arbitrary, user controllable, tolerance but beyond that point may vary from one computer to another. Despite this trade off in generality and precision, the current grid of isochrones generated by DSEP ([Dotter et al., 2008](#)), has been heavily cited since its initial release in 2008, proving that there is a place for a code as specific as DSEP.

## Chapter 4

# Stars as Stellar Laboratories

- Overview of what makes stars so important to human history
- Overview of what makes stars so important to the history of the universe
- General overview of the history of stellar structure
  - History of thought on stars
  - First attempts to describe what stars were
  - Early modern attempts to describe stars (i.e. gravity collapse)
  - Start of modern stellar astrophysics
  - history of stellar structure equations
  - history of computer models
  - history and provenance of DSEP
- Why is it important to understand stellar physics going forward
- Switch gears to talk about GC because of how they are
  - The role GC play in understanding the universe
  - labs to test stellar physics!
- Talk about Jao Gap
  - Talk about the Jao Gap as a stellar laboratory (interiors of low mass stars)

- Talk about the RGBB, again a lab for stellar physics
- brief overview of what will be presented in the thesis

# **Part II**

# **Globular Clusters**



## Chapter 5

# Why Study Globular Clusters



## Chapter 6

# Modeling Globular Clusters

### 6.1 Problems Modeling Globular Clusters



# Chapter 7

## Modeling NGC 2808

### 7.1 Introduction

Globular clusters (GCs) are among the oldest observable objects in the universe (Peng et al., 2011). They are characterized by high densities with typical half-light radii of  $\leq 10$  pc (van den Bergh, 2010), and typical masses ranging from  $10^4$ – $10^5$  M<sub>⊙</sub> (Brodie & Strader, 2006) — though some GCs are significantly larger than these typical values (e.g.  $\omega$ Cen, Richer et al., 1991). GCs provide a unique way to probe stellar evolution (Baumgardt & Makino, 2003), galaxy formation models (Boylan-Kolchin, 2018; Kravtsov & Gnedin, 2005), and dark matter halo structure (Hudson & Robison, 2018).

The traditional view of Globular Clusters was, for a long time, that they consisted of a single stellar population (SSP, in some publications this is referred to as a Simple Stellar Population). This view was supported by spectroscopically uniform heavy element abundances (Carretta et al., 2010; Bastian & Lardo, 2018) accross most clusters (M54 and  $\omega$ Cen are notable exceptions, see Marino et al. (2015) for further details), and the lack of evidence for multiple stellar populations (MPs) in past color-magnitude diagrams of GCs (i.e. Sandage, 1953; Alcaino, 1975). However, over the last 40 years non-trivial star-to-star light-element abundance variations have been observed (i.e. Smith, 1987) and, in the last two decades, it has been definitively shown that most if not all Milky Way GCs have MPs (Gratton et al., 2004, 2012; Piotto et al., 2015). The lack of photometric evidence for MPs can be attributed to

the short color throw available to ground based photometric surveys ([Milone et al., 2017](#)); specifically, lacking UV filters. While MPs are chemically distinct from one another, that distinction is most prominent when observing with  $U$  and  $B$  filters ([Sbordone et al., 2011](#)).

The prevalence of multiple populations in GCs is so distinct that the proposed definitions for what constitutes a globular cluster now often center the existence of MPs. Whereas, people have often tried to categorized objects as GCs through relations between half-light radius, density, and surface brightness profile, in fact many objects which are generally thought of as GCs don't cleanly fit into these cuts ([Peebles & Dicke, 1968](#); [Brown et al., 1991, 1995](#); [Bekki & Chiba, 2002](#)). Consequently, [Carretta et al. \(2010\)](#) proposed a definition of GC based on observed chemical inhomogeneities in their stellar populations. The modern understanding of GCs then is not simply one of a dense cluster of stars which may have chemical inhomogeneities and multiple populations; rather, it is one where those chemical inhomogeneities and multiple populations themselves are the defining element of a GC.

All Milky Way globular clusters older than 2 Gyr studied in detail show populations enriched in He, N, and Na while also being deplete in O and C ([Piotto et al., 2015](#); [Bastian & Lardo, 2018](#)). These light element abundance patterns also are not strongly correlated with variations in heavy element abundance, resulting in spectroscopically uniform Fe abundances between populations. Further, high-resolution spectral studies reveal anti-correlations between N-C abundances, Na-O abundances, and potentially Al-Mg ([Sneden et al., 1992](#); [Gratton et al., 2012](#)). Typical stellar fusion reactions can deplete core oxygen; however, the observed abundances of Na, Al, and Mg cannot be explained by the likes of the CNO cycle ([Prantzos et al., 2007](#)).

Formation channels for these multiple populations remain a point of debate among astronomers. Most proposed formation channels consist of some older, more massive, population of stars polluting the pristine cluster media before a second population forms, now enriched in heavier elements which they themselves could not have generated (for a detailed review see [Gratton et al., 2012](#)). The four primary candidates for these polluters are asymptotic giant branch stars (AGBs, [Ventura et al., 2001](#);

(D’Ercole et al., 2010), fast rotating massive stars (FRMSs, Decressin et al., 2007), super massive stars (SMSs, Denissenkov & Hartwick, 2014), and massive interacting binaries (MIBs, de Mink et al., 2009; Bastian & Lardo, 2018).

Hot hydrogen burning (proton capture), material transport to the surface, and material ejection into the intra-cluster media are features of each of these models and consequently they can all be made to *qualitatively* agree with the observed elemental abundances. However, none of the standard models can currently account for all specific abundances (Gratton et al., 2012). AGB and FRMS models are the most promising; however, both models have difficulty reproducing severe O depletion (Ventura & D’Antona, 2009; Decressin et al., 2007). Moreover, AGB and FRMS models require significant mass loss ( $\sim 90\%$ ) between cluster formation and the current epoch — implying that a significant fraction of halo stars formed in GCs (Renzini, 2008; D’Ercole et al., 2008; Bastian & Lardo, 2015).

In addition to the light-element anti-correlations observed it is also known that younger populations are significantly enhanced in Helium (Piotto et al., 2007, 2015; Latour et al., 2019). Depending on the cluster, Helium mass fractions as high as  $Y = 0.4$  have been inferred (e.g Milone et al., 2015a). However, due to the relatively high and tight temperature range of partial ionization for He it cannot be observed in globular clusters; consequently, the evidence for enhanced He in GCs originates from comparison of theoretical stellar isochrones to the observed color-magnitude-diagrams of globular clusters. Therefore, a careful handling of chemistry is essential when modeling with the aim of discriminating between MPs; yet, only a very limited number of GCs have yet been studied with chemically self-consistent (structure and atmosphere) isochrones (e.g. Dotter et al., 2015, NGC 6752).

NGC 2808 is the prototype globular cluster to host Multiple Populations. Various studies since 2007 have identified that it may host anywhere from 2-5 stellar populations. These populations have been identified both spectroscopically (i.e. ) and photometrically (i.e. ). Note that recent work (Valle et al., 2022) calls into question the statistical significance of the detections of more than 2 populations in the spectroscopic data. Here we present new, chemically self-consistent modeling of the

photometry of the two extreme populations of NGC 2808 identified by Milone et al. (2015a), populations A and E. We use archival photometry from the Hubble UV Globular Cluster Survey (HUGS) (Piotto et al., 2015; Milone et al., 2017) in the F275W and F814W passbands to characterize multiple populations in NGC 2808 (Milone et al., 2015a,b). Additionally, we present a likelihood analysis of the photometric data of NGC 2808 to determine the number of populations present in the cluster.

## 7.2 Stellar Models

We use the Dartmouth Stellar Evolution Program (DSEP, Dotter et al., 2008) to generate stellar models. DSEP is a well-tested, one-dimensional stellar evolution code which includes a mixing length model of convection, gravitational settling, and diffusion. Using the solar composition presented in (Grevesse et al., 2007) (GAS07), MARCS model atmospheres, OPLIB high temperature opacities, and AESOPUS 2.0 low temperature opacities we find a solar calibrated mixing length parameter,  $\alpha_{MLT}$ , of  $\alpha_{MLT} = 1.901$ .

We use DSEP to evolve stellar models ranging in mass from 0.3 to 2.0 solar masses from the zero-age main sequence (ZAMS) to the tip of the red giant branch. Below  $0.7 M_\odot$  we evolve a model every  $0.03 M_\odot$  and above  $0.7 M_\odot$  we evolve a model every  $0.5 M_\odot$ . Additionally, we evolve models over a grid of mixing length parameters from  $\alpha_{MLT} = 1.0$  to  $\alpha_{MLT} = 2.0$  in steps of 0.1. In addition to the mixing length grid the evolved grid of models also has dimensions population (A or E) (Table 7.1) and helium abundance ( $Y = 0.24, 0.27, 0.3, 0.33, 0.36, 0.39$ ). Each model is evolved in DSEP with typical numeric tolerances of one part in  $10^7$ . Each model is allowed a maximum time step of 50 Myr.

For each combination of population,  $Y$ , and  $\alpha_{MLT}$  we use the isochrone generation code first presented in Dotter (2016) to generate a grid of isochrones. The isochrone generation code identified equivalent evolutionary points (EEPs) over a series of masses and interpolates between them. The grid of isochrones generated for this work is available as a digital supplement to this paper. Given the complexity of the parameter space when fitting multiple populations along with the recent warnings

Li	-0.08	—	In	-1.46	—
Be	0.25	—	Sn	-0.22	—
B	1.57	—	Sb	-1.25	—
C	6.87	5.91	Te	-0.08	—
N	6.42	6.69	I	-0.71	—
O	7.87	6.91	Xe	-0.02	—
F	3.43	—	Cs	-1.18	—
Ne	7.12	6.7	Ba	1.05	—
Na	5.11	5.7	La	-0.03	—
Mg	6.86	6.42	Ce	0.45	—
Al	5.21	6.61	Pr	-1.54	—
Si	6.65	6.77	Nd	0.29	—
P	4.28	—	Pm	-99.0	—
S	6.31	5.89	Sm	-1.3	—
Cl	-1.13	4.37	Eu	-0.61	—
Ar	5.59	5.17	Gd	-1.19	—
K	3.9	—	Tb	-1.96	—
Ca	5.21	—	Dy	-1.16	—
Sc	2.02	—	Ho	-1.78	—
Ti	3.82	—	Er	-1.34	—
V	2.8	—	Tm	-2.16	—
Cr	4.51	—	Yb	-1.42	—
Mn	4.3	—	Lu	-2.16	—
Fe	6.37	—	Hf	-1.41	—
Co	3.86	—	Ta	-2.38	—
Ni	5.09	—	W	-1.41	—
Cu	3.06	—	Re	-2.0	—
Zn	2.3	—	Os	-0.86	—
Ga	0.78	—	Ir	-0.88	—
Ge	1.39	—	Pt	-0.64	—
As	0.04	—	Au	-1.34	—
Se	1.08	—	Hg	-1.09	—
Br	0.28	—	Tl	-1.36	—
Kr	0.99	—	Pb	-0.51	—
Rb	0.26	—	Bi	-1.61	—
Sr	0.61	—	Po	-99.0	—
Y	1.08	—	At	-99.0	—
Zr	1.45	—	Rn	-99.0	—
Nb	-0.8	—	Fr	-99.0	—
Mo	-0.38	—	Ra	-99.0	—
Tc	-99.0	—	Ac	-99.0	—
Ru	-0.51	—	Th	-2.2	—
Rh	-1.35	—	Pa	-99.0	—
Pd	-0.69	—	U	-2.8	—

Table 7.1: Relative Metal composition used where  $a(H) = 12$ . Where the relative composition is the same for both populations A and E it is only listed in the population A column for the sake of visual clarity.

in the literature regarding overfitting datasets (e.g. [Valle et al., 2022](#)) we want to develop a more objective way of fitting isochrones to photometry than if we were to mark median ridge line positions by hand.

## 7.3 Chemical Consistency

There are three primary areas in which must the stellar models must be made chemically consistent: the atmospheric boundary conditions, the opacities, and interior abundances. The interior abundances are relatively easily handled by adjusting parameters within our stellar evolutionary code. However, the other two areas are more complicated to bring into consistency. Atmospheric boundary conditions and opacities must both be calculated with a consistent set of chemical abundances outside of the stellar evolution code. For evolution we use the Dartmouth Stellar Evolution Program (DSEP) ([Dotter et al., 2008](#)), a well tested 1D stellar evolution code which has a particular focus on modelling low mass stars ( $\leq 2 M_{\odot}$ )

### 7.3.1 Atmospheric Boundary Conditions

Certain assumptions, primarily that the radiation field is at equilibrium and radiative transport is diffusive ([Salaris & Cassisi, 2005](#)), made in stellar structure codes, such as DSEP, are valid when the optical depth of a star is small. However, in the atmospheres of stars, the number density of particles drops low enough and the optical depth consequently becomes large enough that these assumptions break down, and separate, more physically motivated, plasma modeling code is required. Generally structure code will use tabulated atmospheric boundary conditions generated by these specialized codes ATLAS9 ([Kurucz, 1993](#)), PHEONIX ([Husser et al., 2013](#)), MARCS ([Gustafsson et al., 2008](#)), and MPS-ATLAS ([Kostogryz et al., 2023](#)). Often, as the boundary conditions are both expensive to compute and not the speciality of stellar structure researchers, the boundary conditions are not updated as as light-element interior abundance varies.

One key element when chemically consistently modeling NGC 2808 modeling is the incorporation of new atmospheric models with the same elemental abundances as

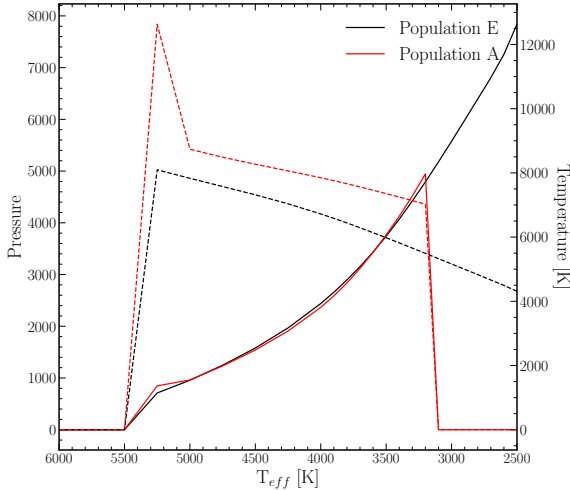


Figure 7.1: Comparison of the MARCS model atmospheres generated for the two extreme populations of NGC 2808. These lines show population A and E with the same Helium abundance; though, we fit a grid of models over various helium abundances. Dashed lines show the temperature of the boundary condition while solid lines show the pressure.

the structure code. We use atmospheres generated from the MARCS grid of model atmospheres (Plez, 2008). MARCS provides one-dimensional, hydrostatic, plane-parallel and spherical LTE atmospheric models (Gustafsson et al., 2008). Model atmospheres are made to match the spectroscopically measured elemental abundances of populations A and E. Moreover, for each populations, atmospheres with various helium mass fractions are generated. These range from  $Y=0.24$  to  $Y=0.36$  in steps of 0.02. All atmospheric models are computed to an optical depth of  $\tau = 100$  where their temperature and pressures serve as boundary conditions for the structure code. A comparison of the pressure and temperature throughout the atmospheres of the two populations with helium abundances representative of literature values is shown in Figure 7.3.1.

### 7.3.2 Opacities

In addition to the atmospheric boundary conditions, both the high and low temperature opacities used by DSEP must be made chemically consistent. Here we use OPLIB high temperature opacity tables (Colgan et al., 2016) retrieved using the TOPS web-interface. Low temperature opacity tables are retrieved from the Aeso-

pus 2.0 web-interface (Marigo & Aringer, 2009; Marigo et al., 2022). Ideally, these opacities would be the same used in the atmospheric models. However, the opacities used in the MARCS models are not publicly available. As such, we use the opacities provided by the TOPS and Aesopus 2.0 web-interfaces.

## 7.4 fidanka

When fitting isochrones to the data we have four main criteria for any method

- The method must be robust enough to work along the entire main sequence, turn off, and much of the subgiant and red giant branches.
- Any method should consider photometric uncertainty in the fitting process.
- The method should be model independent, weighting any number of populations equally.
- The method should be automated and require minimal intervention from the user.

We do not believe that any currently available software is a match for our use case. Therefore, we elect to develop our own software suite, **Fidanka**. **Fidanka** is a python package designed to automate much of the process of measuring fiducial lines in CMDs, adhering to the four criteria we lay out above. Primary features of **Fidanka** may be separated into three categories: fiducial line measurement, stellar population synthesise, and isochrone optimization/fitting. Additionally, there are utility functions which are detailed in the **Fidanka** documentation.

### 7.4.1 Fiducial Line Measurement

**Fidanka** takes a iterative approach to measuring fiducial lines, the first step of which is to make a “guess” as to the fiducial line. . This initial guess is calculated by splitting the CMD into magnitude bins, with uniform numbers of stars per bin (so that bins are cover a small magnitude range over densely populated regions of the CMD while covering a much larger magnitude range in sparsely populated regions

of the CMD, such as the RGB). A unimodal Gaussian distribution is then fit to the color distribution of each bin, and the resulting mean color is used as the initial fiducial line guess. This rough fiducial line will approximately trace the area of highest density. The initial guess will be used to verticalize the CMD so that further algorithms can work in 1-D magnitude bins without worrying about weighting issues caused by varying projections of the evolutionary sequence onto the magnitude axis. Verticalization is performed taking the difference between the guess fiducial line and the color of each star in the CMD.

If `Fidanka` were to simply apply the same algorithm to the verticalized CMD then the resulting fiducial line would likely be a re-extraction of the initial fiducial line guess. To avoid this, we take a more robust, number density based approach, which considers the distribution of stars in both color and magnitude space simultaneously. For each star in the CMD we first use a `introselect` partitioning algorithm to select the 50 nearest stars in F814W vs. F275W-F814W space. To account for the case where the star is at an extreme edge of the CMD, those 50 stars include the star itself (such that we really select 49 stars + 1). We use `qhull`<sup>1</sup>(Barber et al., 1996; ?) to calculate the convex hull of those 50 points. The number density at each star then is defined as  $50/A_{hull}$ , where  $A_{hull}$  is the area of the convex hull. Because we use a fixed number of points per star, and a partitioning algorithm as opposed to a sorting algorithm, this method scales like  $\mathcal{O}(n)$ , where  $n$  is the number of stars in the CMD. This method also intrinsically weights the density of each star equally as the counting statistics per bin are uniform. We are left with a CMD where each star has a defined number density (Figure 7.4.1).

`Fidanka` can now exploit this density map to fit a better fiducial line to the data, as the density map is far more robust to outliers. There are multiple algorithms we implement to fit the fiducial line to the color-density profile in each magnitude bin (Figure 7.4.1); they are explained in more detail in the `Fidanka` documentation. However, of most relevance here is the Bayesian Gaussian Mixture Modeling (BGMM) method. BGMM is a clustering algorithm which, for some fixed number

---

<sup>1</sup><https://www.qhull.com>

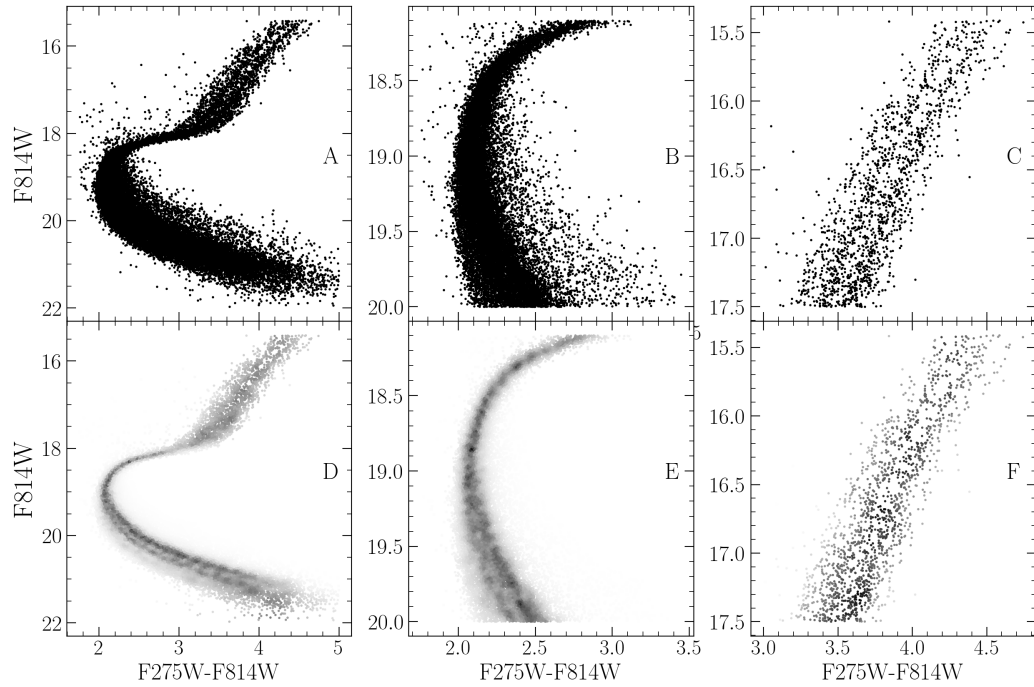


Figure 7.2: Density map demo showing density estimate over different parts of the evolutionary sequence. The left panel shows the density map over the entire evolutionary sequence, while the middle panel shows the density map over the main sequence and the right most panel shows the density map over the RGB. Figures in the top row are the raw CMD, while figures in the bottom row are colored by the density map.

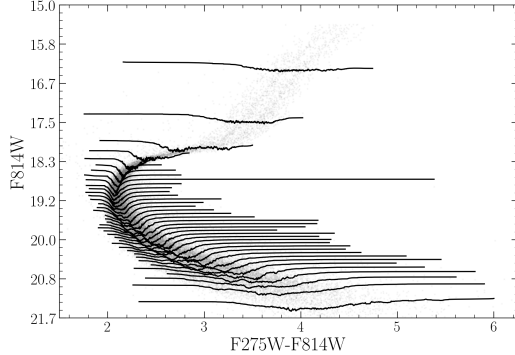


Figure 7.3: CMD where points are colored by density. Lines show the density-color profile in each magnitude bin. In this figure adaptive binning targeted 1000 stars per bin

of  $n$ -dimensional Gaussian distributions,  $K$ , determines the mean, covariance, and mixing probability (somewhat analogous to amplitude) of each  $k^{th}$  distribution, such that the local lower bound of the evidence of each star belonging strongly to a single distribution is maximized.

Maximization is preformed using the Dirichlet process, which is a non-parametric Bayesian method of determining the number of Gaussian distributions,  $K$ , which best fit the data (Ferguson, 1973; Pedregosa et al., 2011). Use of the Dirichlet process allows for dynamic variation in the number of inferred populations from magnitude bin to magnitude bin. Specifically, populations are clearly visually separated from the lower main sequence through the turn off; however, at the turn off and throughout much of the subgiant branch, the two visible populations overlap due to their extremely similar ages (i.e. Jordán et al., 2002). The Dirichlet process allows for the BGMM method to infer a single population in these regions, while inferring two populations in regions where they are clearly separated. More generally, the use of the Dirichlet process removes the need for a prior on the exact number of populations to fit. Rather, the user specifies a upper bound on the number of populations within the cluster. An example bin ( $F814W = 20.6$ ) is shown in Figure 7.4.

**Fidanka**'s BGMM method first breaks down the verticalized CMD into magnitude bins with uniform numbers of stars per bin (here we adopt 250). Any stars left over are placed into the final bin. For each bin a BGMM model with a maximum of 5

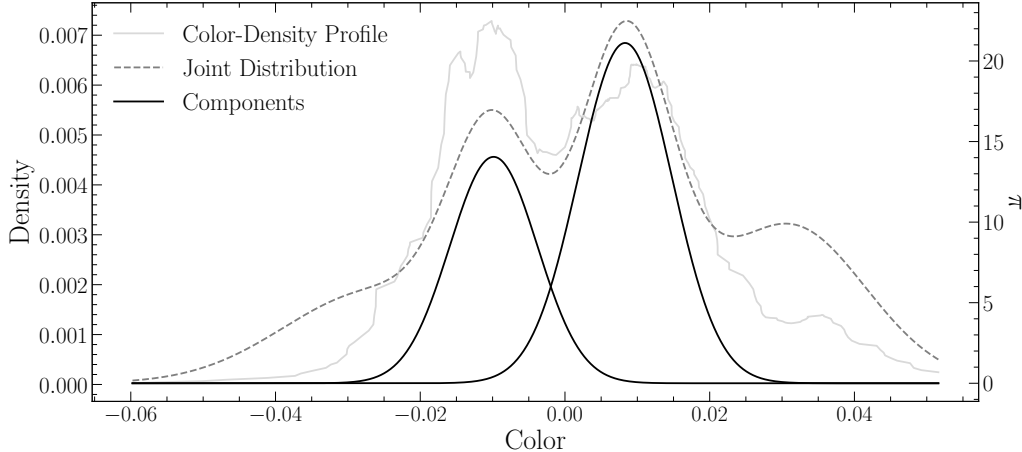


Figure 7.4: Example of BGMM fit to a magnitude bin. The grey line shows the underlying color-density profile, while the black dashed-line shows the joint distribution of each BGMM component. The solid black lines show the two selected components.

populations is fit to the color density profile. The number of populations is then inferred from the weighting parameter (the mixing probability) of each population. If the weighting parameter of any  $k^{th}$  components less than [0.05](#), then that component is considered to be spurious and removed. Additionally, if the number of populations in the bin above and the bin below are the same, then the number of populations in the current bin is forced to be the same as the number of populations in the bin above. Finally, the initial guess fiducial line is added back to the BGMM inferred line. Figure 7.5 shows the resulting fiducial line(s) in each magnitude bin for both a verticalized CMD and a non verticalized CMD.

This method of fiducial line extraction effectively discriminated between multiple populations long the main sequence and RGB of a cluster, while simultaneously allowing for the presence of a single population along the MSTO and subgiant branch.

We can adapt this density map based BGMM method to consider photometric uncertainties by adopting a simple Monte Carlo approach. Instead of measuring the fiducial line(s) a single time, **Fidanka** can measure the fiducial line(s) many times, resampling the data with replacement each time. For each resampling **Fidanka** adds a random offset to each filter based on the photometric uncertainties of each star. From these  $n$  measurements the mean fiducial line for each sequence can be identified

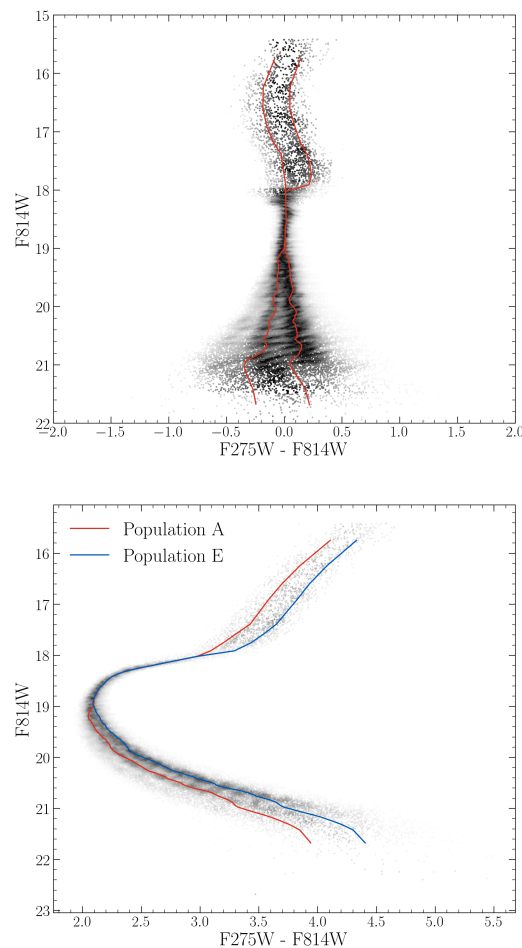


Figure 7.5: CMD where points are colored by density. Line trace the inferred fiducial line(s) in each magnitude bin.

along with upper and lower bound confidence intervals in each magnitude bin.

#### 7.4.2 Stellar Population Synthesis

In addition to measuring fiducial lines, **Fidanka** also includes a stellar population synthesise module. This module is used to generate synthetic CMDs from a given set of isochrones. This is of primary importance for binary population modelling. The module is also used to generate synthetic CMDs for the purpose of testing the fiducial line extraction algorithms against priors.

**Fidanka** uses MIST formatted isochrones ([Dotter, 2016](#)) as input along with distance modulus, B-V color excess, binary mass fraction, and bolometric corrections. An arbitrarily large number of isochrones may be used to define an arbitrary number of populations. Synthetic stars are samples from each isochrone based on a definable probability (for example it is believed that  $\sim 90\%$  of stars in globular clusters are younger population (e.g. [Suntzeff & Kraft, 1996](#); [Carretta, 2013](#))). Based on the metallicity,  $\mu$ , and E(B-V) of each isochrone, bolometric corrections are taken from bolometric correction tables. Where bolometric correction tables do not include exact metallicities or extinctions a linear interpolation is preformed between the two bounding values.

#### 7.4.3 Isochrone Optimization

The optimization routines in **Fidanka** will find the best fit distance modulus, B-V color excess, and binary number fraction for a given set of isochrones. If a single isochrone is provided then the optimization is done by minimizing the  $\chi^2$  of the perpendicular distances between an isochrone and a fiducial line. If multiple isochrones are provided then those isochrones are first used to run stellar population synthesis and generate a synthetic CMD. The optimization is then done by minimizing the  $\chi^2$  of both the perpendicular distances between and widths of the observed fiducial line and the fiducial line of the synthetic CMD.

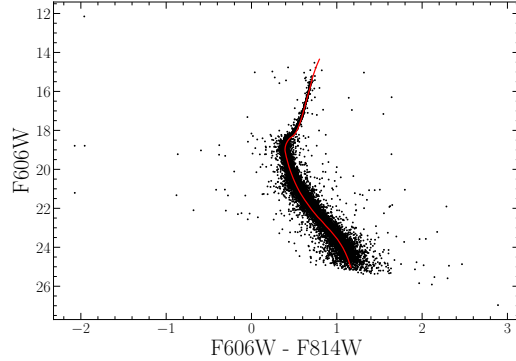


Figure 7.6: Synthetic population generated by fidanka at 10000pc with  $E(B-V) = 0$ , and an age of 12 Gyr along with the best fitting isochrone. The best fit paremeters are derived to be  $\mu u = 15.13$ ,  $E(B-V)=0.001$ , and an age of 12.33 Gyr.

#### 7.4.4 Fidanka Testing

In order to validate fidanka we have run a series of injection recovery tests using **Fidanka**'s population synthesis routines to build various synthetic populations and **Fidanka**'s fiducial measurement routines to recover these populations. Each population was generated using the initial mass function given in (Milone et al., 2012) for the redmost population ( $\alpha = -1.2$ ). Further, every population was given a binary population fraction of 10%, distance uniformly sampled between 5000pc and 15000pc, and a B-V color excess uniformly sampled between 0 and 0.1. Finally, each synthetic population was generated using a fixed age uniformly sampled between 7 Gyr and 14 Gyr. An example synthetic population along with its associated best fit isochrone are shown in Figure 7.6.

For each trial we use **Fidanka** to measure the fiducial line and then optimize that fiducial line against the originating isochrone to esimate distance modulus, age, and color B-V excess. Figure 7.7 is built from 1000 runs of these trials and show the mean and width of the percent error distributions for  $\mu$ ,  $E(B - V)$ , and age. In general **Fidanka** is able to recover distance modulii effectively with age and  $E(B-V)$  reovery falling in line with other literature that does not cosider the CMD outside of the main sequence, main sequence turn off, sub giant, and red giant branches; specifically, it should be noted that **Fidanka** is not setup to model the horizontal branch.

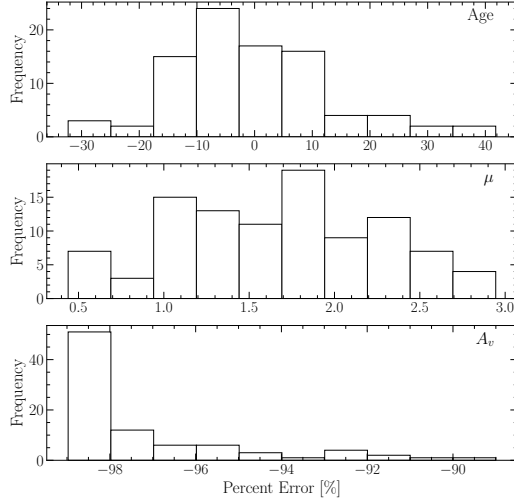


Figure 7.7: Percent Error distribution for each of the three deriver parameters. Note that these values will be sensitive to the magnitude uncertainties of the photometry. Here we made use of the ACS artificial star tests to estimate the uncertainties. **Note that currently this is built with 100 runs, these take a long time so currently re running with 1000 runs.**

## 7.5 Isochrone Fitting

We fit pairs of isochrones to the HUGS data for NGC 2808 using `Fidanka`, as described in §7.4. Two isochrones, one for Population A and one for Population E are fit simultaneously. These isochrones are constrained to have distance modulus,  $\mu$ , and color excess,  $E(B-V)$  which agree to within 1%. Moreover, we constrain the mixing length,  $\alpha_{ML}$ , for any two isochrones in a set to be within 0.5 of one and other. For every isochrone in the set of combination of which fulfilling these constraints  $\mu$ ,  $E(B-V)$ ,  $Age_A$ , and  $Age_B$  are optimized to reduce the  $\chi^2$  distance between the fiducial lines and the isochrones. Because we fit fiducial lines directly, we do not need to consider the binary population fraction,  $f_{bin}$ , as a free parameter.

The best fit isochrones are shown in Figure 7.6 and optimized parameters for these are presented in Table 7.6. We find helium mas fractions which are consistent with those identified in past literature (e.g. Milone et al., 2015a). Note that our helium mass fraction grid has a spacing of 0.03 between grid points and we are therefore unable to resolve between certain proposed helium mass fractions for the younger sequence (for example between 0.37 and 0.39).

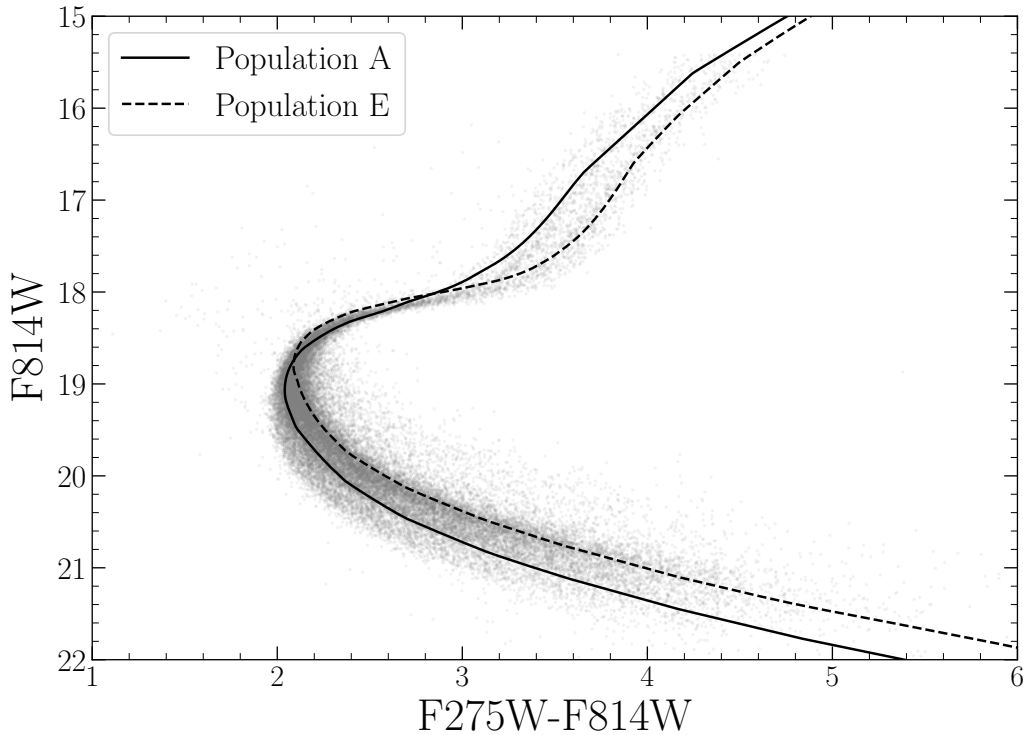


Figure 7.8: Best fit isochrone results for NGC 2808.

population	age [Gyr]	distance modulus	extinction [mag]	$\text{Y}$	$\alpha_{ML}$	$\chi^2_\nu$
A	12.3	14.91	0.54	0.24	1.901	0.014
E	14.3	14.96	0.54	0.39	1.750	0.017

Table 7.2: Best fit parameters derived from fitting isochrones to the fiducial lines derived from the NCG 2808 photometry.

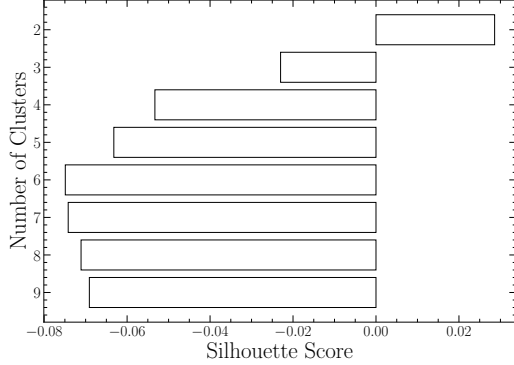


Figure 7.9: Silhouette analysis for NGC 2808 F275W-F814W photometry. The Silhouette scores are an average of score for each magnitude bin. Positive scores indicate that the clustering algorithm produced well distinguished clusters while negative scores indicate clusters which are not well distinguished.

Past literature (e.g. [Milone et al., 2015a, 2018](#)) have found helium mass fraction variation from the low redmost to bluemost populations of  $\sim 0.12$ . Here we find a helium mass fraction variation of 0.15 which, given the spacing of the helium grid we use **is consistent with these past results**.

### 7.5.1 The Number of Populations in NGC 2808

In order to estimate the number of populations which ideally fit the NGC 2808 F275W-F814W photometry without overfitting the data we make use of silhouette analysis ([Rousseeuw, 1987](#), and in a similar manner to how [Valle et al. \(2022\)](#) perform their analysis of spectroscopic data). We find the average silhouette score for all tagged clusters identified using BGMM in all magnitude bins over the CMD using the standar python module `sklearn`. Figure 7.9 shows the silhouette analysis results and that 2 populations fit the photometry most ideally. This is in line with what our BGMM model predicts for the majority of the the CMD.

### 7.5.2 ACS-HUGS Photometric Zero Point Offset

The Hubble legacy archive photometry used in this work is calibrated to the Vega magnitude system. However, we have found that the photometry has a systematic offset of  $\sim 0.026$  magnitudes in the F814W band when compared to the same stars in the ACS survey (Figure 7.5.2). The exact cause of this offset is unknown, but it

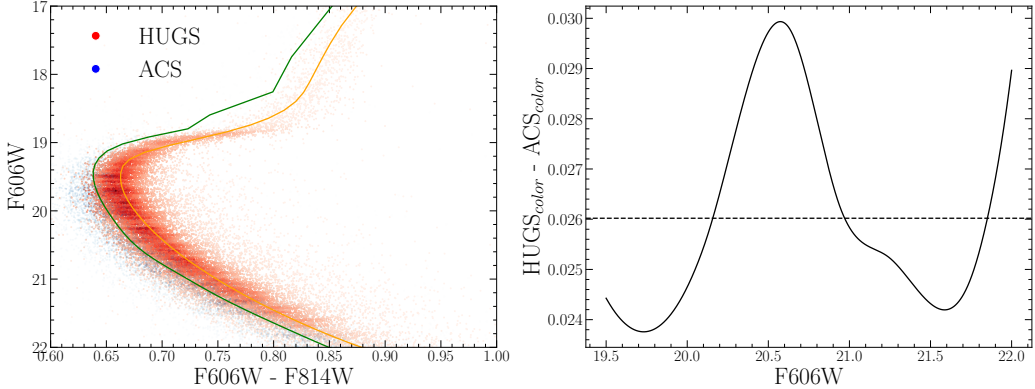


Figure 7.10: (left) CMD showing the photometric offset between the ACS and HUGS data for NGC 2808. CMDs have been randomly subsampled and colored by point density for clarity. (right) Mean difference between the color of the HUGS and ACS fiducial lines at the same magnitude. Note that the ACS data is systematically bluer than the HUGS data.

is likely due to a difference in the photometric zero point between the two surveys. A full correction of this offset would require a careful re-reduction of the HUGS photometry, which is beyond the scope of this work. We instead recognize a 0.02 inherent uncertainty in the inferred magnitude of any fit when comparing to the ACS survey. This uncertainty is small when compared to the uncertainty in the distance modulus and should not affect the conclusion of this paper.

The observed photometric offset between ACS and HUGS reductions introduces a systematic uncertainty when comparing parameters derived from isochrone fits to ACS data vs those fit to HUGS data. Specifically, this offset introduces a  $\sim$ AGE Gyr uncertainty. Moreover, for two isochrone of the same age, only separated by helium mass fraction, a shift of the main sequence turn off is also expected. Figure 7.11 shows this shift. Note a change in the helium mass fraction of a model by 0.03 results in an approximate 0.08 magnitude shift to the main sequence turn off location. This means that the mean 0.026 magnitude offset we find in between ACS and HUGS data corresponds to an additional approximate 0.01 uncertainty in the derived helium mass fraction when comparing between these two datasets.

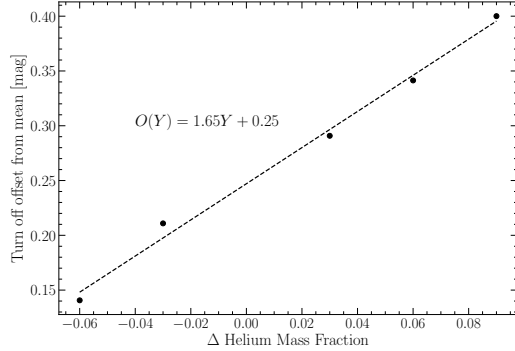


Figure 7.11: Main sequence turn off magnitude offset from a guage helium mass fraction ( $Y=0.30$  chosen). All main sequence turn off locations are measured at 12.3 Gyr [Should I make these contour surfaces for various ages?](#)

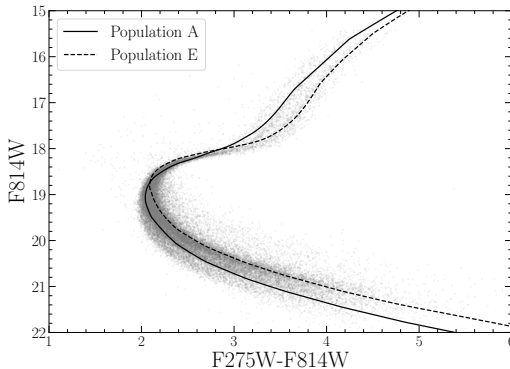


Figure 7.12: Best fit isochrone results for NGC 2808.

## 7.6 Results

Using `Fidanka` we fit pairs of Population A + E isochrones to the HUGS data for NGC 2808. Each pair of isochrones is allowed to vary in distance modulus, reddening, relative helium mass fraction (A/E), and age. Any population pairs which vary by more than 1% in distance modulus or B-V color excess are rejected. The  $\chi^2$  distribution for the isochrone pairs is shown in Figure [FIGURE]. The best fit isochrones are shown in Figure 7.6 and optimized parameters for these are presented in Table [TABLE].

Need to make the chi2 dist plot still. Have all these values but need to figure out best way to visualize it

population	age [Gyr]	distance modulus	extinction mag	Y	$\alpha_{ML}$	$\chi^2_\nu$
A	12.3	14.91	0.54	0.24	1.901	0.014
E	14.3	14.96	0.54	0.39	1.750	0.017

Table 7.3: Best fit parameters derived from fitting isochrones to the fiducial lines derived from the NCG 2808 photometry.

Currently are still seeing a discontinuity in the isochrone below the MSTO. This must be addressed before submission.

### 7.6.1 The Number of Populations in NGC 2808

`Fidanka` provides a somewhat straightforward way to estimate the number of populations expected in a given magnitude bin given the observations. See Section 7.4 for specific implementation details. Here we perform an analysis of the number of populations seen in the NGC 2808 F814W-F274W vs F814W color-magnitude diagram. We find that for the majority of the main sequence and red giant branches BGMM prefers two populations; whereas, near the main sequence turn off and on the majority of the subgiant branches BGMM prefers a single population model.

[FIGURE SHOWING BGMM population probability]

## 7.7 Conclusion

Here we have performed the first chemically self-consistent modeling of the Milky Way Globular Cluster NGC 2808. We find that, updated atmospheric boundary conditions and opacity tables do not have a significant effect on the inferred helium abundances of multiple populations. Specifically, we find that the older stellar population, population A, has a helium mass fraction of 0.24, while the older population, E, has a helium mass fraction of 0.39.

Further, we introduce a new software suite for globular cluster science, `Fidanka`, which has been released under a permissive open source license. `Fidanka` aims to provide a statistically robust set of tools for estimating the parameters of multiple populations within globular clusters.



## Chapter 8

# Modeling NGC 6752



## Part III

# Magnetic Fields and the Gaia M dwarf Gap



# Chapter 9

## Magnetic Fields In M Dwarfs

### 9.1 Magnetic Activity in M dwarfs

M-dwarfs are the most numerous stars in our galaxy. Some planet search campaigns have focused on M-dwarfs due to the relative ease of detecting small planets in their habitable zones (e.g. Nutzman & Charbonneau, 2008); however, spun-up M-dwarfs are more magnetically active when compared to larger and hotter stars (Hawley & Pettersen, 1991; Delfosse et al., 1998; Schmidt et al., 2014). The increase in activity may accelerate the stripping of an orbiting planet's atmosphere (e.g. Owen & Mohanty, 2016), and may dramatically impact habitability (Shields et al., 2016). Therefore, it is essential to understand the magnetic activity of M-dwarfs in order to constrain the potential habitability and history of the planets that orbit them. Additionally, rotation and activity may impact the detectability of hosted planets (e.g. Robertson et al., 2014; Newton et al., 2016; Vanderburg et al., 2016).

Robust theories explaining the origin of solar-like magnetic fields exist and have proven extensible to other regions of the main sequence (Charbonneau, 2014). The classical  $\alpha\Omega$  dynamo relies on differential rotation between layers of a star to stretch a seed poloidal field into a toroidal field (Parker, 1955; Cameron et al., 2017). Magnetic buoyancy causes the toroidal field to rise through the star. During this rise, turbulent helical stretching converts the toroidal field back into a poloidal field (Parker, 1955). Seed fields may originate from the stochastic movement of charged particles within a star's atmospheres.

In non-fully convective stars the initial conversion of the toroidal field to a poloidal field is believed to take place at the interface layer between the radiative and convective regions of a star — the tachocline (Noyes et al., 1984; Tomczyk et al., 1996; Dikpati & Charbonneau, 1999). The tachocline has two key properties that allow it to play an important role in solar type magnetic dynamos: 1), there are high shear stresses, which have been confirmed by astroseismology (Thompson et al., 1996), and 2), the density stratification between the radiative and convective zones serves to “hold” the newly generated toroidal fields at the tachocline for an extended time. Over this time, the fields build in strength significantly more than they would otherwise (Parker, 1975). This theory does not trivially extend to mid-late M-dwarfs, as they are believed to be fully convective and consequently do not contain a tachocline (?). Moreover, fully convective M-dwarfs are not generally expected to exhibit internal differential rotation (e.g. Barnes et al., 2004, 2005), though, some models do produce it (Gastine et al., 2014).

Currently, there is no single accepted process that serves to build and maintain fully convective M-dwarf magnetic fields in the same way that the  $\alpha$  and  $\Omega$  processes are presently accepted in solar magnetic dynamo theory. Three-dimensional magneto anelastic hydrodynamical simulations have demonstrated that local fields generated by convective currents can self organize into large scale dipolar fields. These models indicate that for a fully convective star to sustain a magnetic field it must have a high degree of density stratification — density contrasts greater than 20 at the tachocline — and a sufficiently large magnetic Reynolds number<sup>1</sup>.

An empirical relation between the rotation rate and the level of magnetic activity has been demonstrated in late-type stars (Skumanich, 1972; Pallavicini et al., 1981). This is believed to be a result of faster rotating stars exhibiting excess non-thermal emission from the upper chromosphere or corona when compared to their slower rotating counterparts. This excess emission is due to magnetic heating of the upper atmosphere, driven by the underlying stellar dynamo. **The faster a star rotates, up to some saturation threshold, the more such emission is expected.**

---

<sup>1</sup>The Reynolds Number is the ratio of magnetic induction to magnetic diffusion; consequently, a plasma with a larger magnetic Reynolds number will sustain a magnetic field for a longer time than a plasma with a smaller magnetic Reynolds number.

However, the dynamo process is not dependent solely on rotation; rather, it depends on whether the contribution from the rotational period ( $P_{rot}$ ) or convective motion — parameterized by the convective overturn time scale ( $\tau_c$ ) — dominates the motion of a charge packet within a star. Therefore, the Rossby Number ( $Ro = P_{rot}/\tau_c$ ) is often used in place of the rotational period as it accounts for both.

The rotation-activity relation was first discovered using the ratio of X-ray luminosity to bolometric luminosity ( $L_X/L_{bol}$ ) (Pallavicini et al., 1981) and was later demonstrated to be a more general phenomenon, observable through other activity tracers, such as Ca II H&K emission (Vilhu, 1984). This relation has a number of important structural elements. Noyes et al. (1984) showed that magnetic activity as a function of Rossby Number is well modeled as a piecewise power law relation including a saturated and non-saturated regime. In the saturated regime, magnetic activity is invariant to changes in Rossby Number; in the non-saturated regime, activity decreases as Rossby Number increases. The transition between the saturated and non-saturated regions occurs at  $Ro \sim 0.1$  (e.g. Wright et al., 2011). Recent evidence may suggest that, instead of an unsaturated region where activity is fully invariant to rotational period, activity is more weakly, but still positively, correlated with rotation rate (Mamajek & Hillenbrand, 2008; Reiners et al., 2014; Lehtinen et al., 2020; Magaudda et al., 2020).

Previous studies of the Ca II H&K rotation-activity relation (e.g. Vaughan et al., 1981; Suárez Mascareño et al., 2015; Astudillo-Defru et al., 2017; Houdebine et al., 2017) have focused on spectral ranges which both extend much earlier than M-dwarfs and which do not fully probe late M-dwarfs. **Other studies have relied on  $v \sin(i)$  measurements (e.g. Browning et al., 2010; Houdebine et al., 2017), which are not sensitive to the long rotation periods reached by slowly rotating, inactive mid-to-late type M dwarfs (70-150 days: Newton et al., 2016).** Therefore, these studies can present only coarse constraints on the rotation activity relation in the fully convective regime. The sample we present in this paper is focused on mid-to-late type M dwarfs, **with photometrically measured rotational periods**, while maintaining of order the same number of targets as previous

studies. Consequently, we provide much finer constraints on the rotation–activity relation in this regime.

We present a high resolution spectroscopic study of 53 mid-late M-dwarfs. We measure Ca II H&K strengths, quantified through the  $R'_{HK}$  metric, which is a bolometric flux normalized version of the Mount Wilson S-index. These activity tracers are then used in concert with photometrically determined rotational periods, compiled by [Newton et al. \(2017\)](#), to generate a rotation–activity relation for our sample. This paper is organized as follows: Section 9.2 provides an overview of the observations and data reduction, Section 9.3 details the analysis of our data, and Section 11.2 presents our results and how they fit within the literature.

## 9.2 Observations & Data Reduction

We **initially** selected a sample of 55 mid-late M-dwarfs from targets of the MEarth survey ([Berta et al., 2012](#)) to observe. Targets were selected based on high proper motions and availability of a previously measured photometric rotation period, or an expectation of a measurement based on data available from MEarth-South at the time. These rotational periods were derived photometrically (e.g. [Newton et al., 2016](#); [Mann et al., 2016](#); [Medina et al., 2020](#)). For star 2MASS J06022261-2019447, which was categorized as an “uncertain detection” from MEarth photometry by [Newton et al. \(2018\)](#), including new data from MEarth DR10 we find a period of 95 days. This value was determined following similar methodology to [Irwin et al. \(2011\)](#) and [Newton et al. \(2016, 2018\)](#), and is close to the reported candidate period of 116 days. References for all periods are provided in the machine readable version of Table 9.1.

High resolution spectra were collected from March to October 2017 using the Magellan Inamori Kyocera Echelle (MIKE) spectrograph on the 6.5 meter Magellan 2 telescope at the Las Campanas Observatory in Chile. MIKE is a high resolution double echelle spectrograph with blue and red arms. Respectively, these cover wavelengths from 3350 - 5000 Å and 4900-9500 Å ([Bernstein et al., 2003](#)). We collected data using a 0.75x5.00” slit resulting in a resolving power of 32700. Each science target was observed an average of four times with mean integration times per obser-

vation ranging from 53.3 to 1500 seconds. **Ca II H&K lines were observed over a wide range of signa-to-noise ratios, from  $\sim 5$  up to  $\sim 240$  with mean and median values of 68 and 61 respectively.**

We use the CarPy pipeline (Kelson et al., 2000; Kelson, 2003) to reduce our blue arm spectra. CarPy’s data products are wavelength calibrated, blaze corrected, and background subtracted spectra comprising 36 orders. We shift all resultant target spectra into the rest frame by cross correlating against a velocity template spectrum. For the velocity template we use an observation of Proxima Centari in our sample. This spectrum’s velocity is both barycentrically corrected, using astropy’s `SkyCoord` module (Astropy Collaboration et al., 2018), and corrected for Proxima Centari’s measured radial velocity,  $-22.4 \text{ km s}^{-1}$  (Torres et al., 2006). Each echelle order of every other target observation is cross correlated against the corresponding order in the template spectra using `specutils template correlate` function (Earl et al., 2021). Velocity offsets for each order are inferred from a Gaussian fit to the correlation vs. velocity lag function. For each target, we apply a three sigma clip to list of echelle order velocities, visually verifying this clip removed low S/N orders. We take the mean of the sigma-clipped velocities Finally, each wavelength bin is shifted according to its measured velocity.

Ultimately, two targets (2MASS J16570570-0420559 and 2MASS J04102815-5336078) had S/N ratios around the Ca II H&K lines which were too low to be of use, reducing the number of  $R'_{HK}$  measurement we can make from 55 to 53.

### 9.3 Analysis

Since the early 1960s, the Calcium Fraunhauer lines have been used as chromospheric activity tracers (Wilson, 1963). Ca II H&K lines are observed as a combination of a broad absorption feature originating in the upper photosphere along with a narrow emission feature from non-thermal heating of the upper chromosphere (Catalano & Marilli, 1983). Specifically, the ratio between emission in the Ca II H&K lines and flux contributed from the photosphere is used to define an activity metric known as the S-index (Wilson, 1968). The S-index increases with increasing magnetic activity.

The S-index is defined as

$$S = \alpha \frac{f_H + f_K}{f_V + f_R} \quad (9.1)$$

where  $f_H$  and  $f_K$  are the integrated flux over triangular passbands with a full width at half maximum of 1.09 Å centered at 3968.47 Å and 3933.66 Å, respectively. The values of  $f_V$  and  $f_R$  are integrated, top hat, broadband regions. They approximate the continuum (Figure 9.1) and are centered at 3901 Å and 4001 Å respectively, with widths of 20 Å each. Finally,  $\alpha$  is a scaling factor with  $\alpha = 2.4$ .

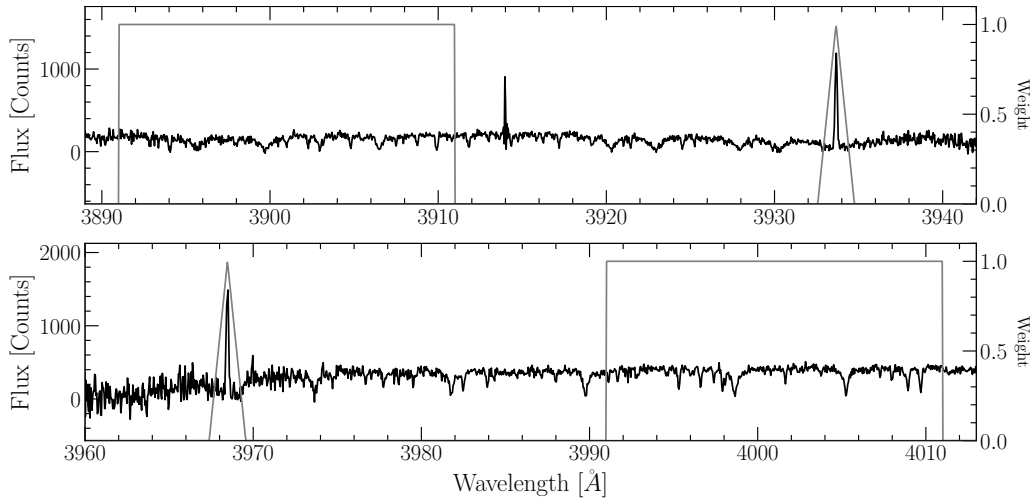


Figure 9.1: Spectrum of 2MASS J06105288-4324178 overplotted with the S index bandpasses. (top) V band and Ca II K emission line. (bottom) Ca II H emission line and R band. Note that the rectangular and triangular regions denote both the wavelength range of the band and the relative weight assigned to each wavelength in the band while integrating.

Following the procedure outlined in Lovis et al. (2011) we use the mean flux per wavelength interval,  $\tilde{f}_i$ , as opposed to the integrated flux over each passband when computing the S-index. This means that for each passband,  $i$ , with a blue most wavelength  $\lambda_{b,i}$  and a red most wavelength  $\lambda_{r,i}$ ,  $\tilde{f}_i$  is the summation of the product of flux ( $f$ ) and weight ( $w_i$ ) over the passband.

$$\tilde{f}_i = \frac{\sum_{l=\lambda_{b,i}}^{\lambda_{r,i}} f(l)w_i(l)}{\lambda_{r,i} - \lambda_{b,i}} \quad (9.2)$$

where  $w_i$  represents the triangular passband for  $f_H$  &  $f_K$  and the tophat for  $f_V$  &  $f_R$ .

Additionally, the spectrograph used at Mount Wilson during the development of the S-index exposed the H & K lines for eight times longer than the continuum of the spectra. Therefore, for a modern instrument that exposes the entire sensor simultaneously, there will be 8 times less flux in the Ca II H&K passbands than the continuum passbands than for historical observations. This additional flux is accounted for by defining a new constant  $\alpha_H$ , defined as:

$$\alpha_H = 8\alpha \left( \frac{1.09 \text{ \AA}}{20 \text{ \AA}} \right) \quad (9.3)$$

Therefore, S-indices are calculated here not based on the historical definition given in Equation 9.1; rather, the slightly modified version:

$$S = \alpha_H \frac{\tilde{f}_H + \tilde{f}_K}{\tilde{f}_V + \tilde{f}_R} \quad (9.4)$$

The S-index may be used to make meaningful comparisons between stars of similar spectral class; however, it does not account for variations in photospheric flux and is therefore inadequate for making comparisons between stars of different spectral classes. The  $R'_{HK}$  index (Middelkoop, 1982) is a transformation of the S-index intended to remove the contribution of the photosphere.

$R'_{HK}$  introduces a bolometric correction factor,  $C_{cf}$ , developed by Middelkoop (1982) and later improved upon by Rutten (1984). Calibrations of  $C_{cf}$  have focused on FGK-type stars using broad band color indices, predominately B-V. However, these FGK-type solutions do not extend to later type stars easily as many mid-late M-dwarfs lack B-V photometry. Consequently,  $C_{cf}$  based on B-V colors were never calibrated for M-dwarfs as many M-dwarfs lack B and V photometry. Suárez Mascareño et al. (2016) provided the first  $C_{cf}$  calibrations for M-dwarfs using the more appropriate color index of  $V - K$ . The calibration was later extended by Astudillo-Defru et al. (2017), which we adopt here.

Generally  $R'_{HK}$  is defined as

$$R'_{HK} = K\sigma^{-1}10^{-14}C_{cf}(S - S_{phot}) \quad (9.5)$$

where K is a factor to scale surface fluxes of arbitrary units into physical units; the current best value for K is taken from [Hall et al. \(2007\)](#),  $K = 1.07 \times 10^6 \text{ erg cm}^{-2} \text{ s}^{-1}$ .  $S_{phot}$  is the photospheric contribution to the S-index; in the spectra this manifests as the broad absorption feature wherein the narrow Ca II H&K emission resides.  $\sigma$  is the Stephan-Boltzmann constant. If we define

$$R_{phot} \equiv K\sigma^{-1}10^{-14}C_{cf}S_{phot} \quad (9.6)$$

then we may write  $R'_{HK}$  as

$$R'_{HK} = K\sigma^{-1}10^{-14}C_{cf}S - R_{phot}. \quad (9.7)$$

We use the color calibrated coefficients for  $\log_{10}(C_{cf})$  and  $\log_{10}(R_{phot})$  presented in Table 1 of [Astudillo-Defru et al. \(2017\)](#).

We estimate the uncertainty of  $R'_{HK}$  as the standard deviation of a distribution of  $R'_{HK}$  measurements from 5000 Monte Carlo tests. For each science target we offset the flux value at each wavelength bin by an amount sampled from a normal distribution. The standard deviation of this normal distribution is equal to the estimated error at each wavelength bin. These errors are calculated at reduction time by the pipeline. **The  $R'_{HK}$  uncertainty varies drastically with signal-to-noise; targets with signal-to-noise ratios  $\sim 5$  have typical uncertainties of a few percent whereas targets with signal-to-noise ratios  $\sim 100$  have typical uncertainties of a few tenth of a percent.**

### 9.3.1 Rotation and Rossby Number

The goal of this work is to constrain the rotation activity relation; therefore, in addition to the measured  $R'_{HK}$  value, we also need the rotation of the star. As mentioned, one of the selection criteria for targets was that their rotation periods were already measured; however, ultimately **6** of the 53 targets with acceptable S/N did not have well constrained rotational periods. We therefore only use the remaining 47 targets to fit the rotation-activity relation.

In order to make the most meaningful comparison possible we transform rotation period into Rossby Number . This transformation was done using the convective overturn timescale,  $\tau_c$ , such that the Rossby Number,  $Ro = P_{rot}/\tau_c$  . To first order  $\tau_c$  can be approximated as 70 days for fully-convective M-dwarfs (Pizzolato et al., 2000). However, Wright et al. (2018) Equation (5) presents an empirically calibrated expression for  $\tau_c$ . This calibration is derived by fitting the convective overturn timescale as a function of color index, in order to minimize the horizontal offset between stars of different mass in the rotation-activity relationship. The calibration from Wright et al. (2018) that we use to find convective overturn timescales and subsequently Rossby numbers is:

$$\log_{10}(\tau_c) = (0.64 \pm 0.12) + (0.25 \pm 0.08)(V - K) \quad (9.8)$$

We adopt symmetric errors for the parameters of Equation 9.8 equal to the larger of the two anti-symmetric errors presented in Wright et al. (2018) Equation 5.

## 9.4 Rotation–Activity Relation

We show our rotation-activity relation in Figures 9.2 & 9.3. Note that errors are shown in both figures; however, they render smaller than the data point size. Ca II H&K is also known to be time variable (e.g. Baroch et al., 2020; Perdelwitz et al., 2021), which is not captured in our single-epoch data. There is one target cut off by the domain of this graph, 2MASS J10252645+0512391. This target has a measured  $v\sin i$  of  $59.5 \pm 2.1$   $\text{km s}^{-1}$  (Kesseli et al., 2018) and is therefore quite rotationally broadened, which is known to affect  $R'_{HK}$  measurements (Schröder et al., 2009, figure 8). The data used to generate this figure is given in Table 9.1. Table 9.1 includes uncertainties, the  $R'_{HK}$  measurements for stars which did not have photometrically derived rotational periods in MEarth, and data for 2MASS J10252645+0512391

We find a rotation activity relationship qualitatively similar to that presented in

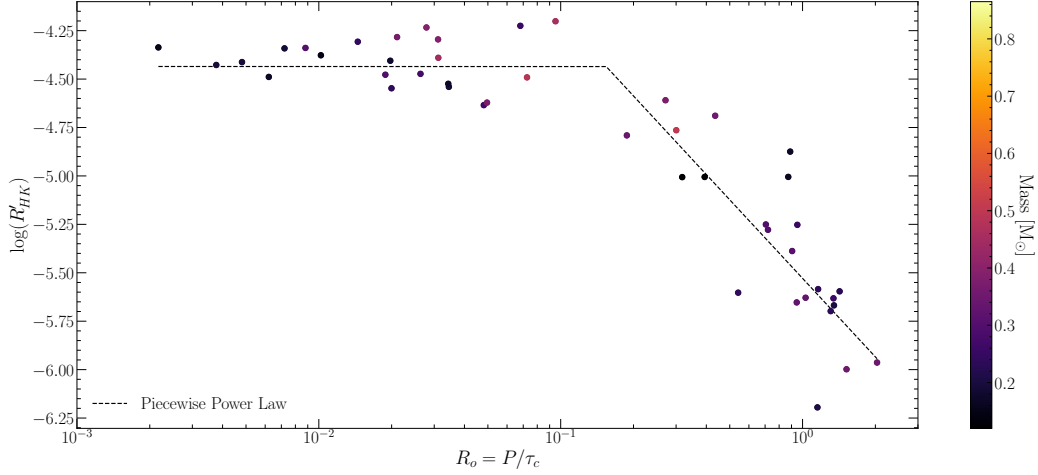


Figure 9.2: Rotation activity relation from this work. The color axis gives each stars mass. The dashed line is the best fit to our data set.

[Astudillo-Defru et al. \(2017\)](#). Our rotation activity relationship exhibits both the expected saturated and unsaturated regimes — the flat region at  $Ro < Ro_s$  and the sloped region at  $Ro \geq Ro_s$  respectively. We fit the rotation activity relation given in Equation 9.9 to our data using Markov Chain Monte Carlo (MCMC), implemented in `pymc` ([Salvatier et al., 2016](#)).

$$\log(R'_{HK}) = \begin{cases} \log(R_s) & Ro < Ro_s \\ k \log(Ro) + \log(R_s) - k \log(Ro_s) & Ro \geq Ro_s \end{cases} \quad (9.9)$$

$Ro_s$  is the Rossby number cutoff between the saturated and unsaturated regime.  $R_s$  is the maximum, saturated, value of  $R'_{HK}$  and  $k$  is the index of the power law when  $Ro \geq Ro_s$ . **Due to the issues measuring  $R'_{HK}$  for high  $vsini$  targets discussed above, we exclude 2MASS J10252645+0512391 from this fit.** All logarithms are base ten unless another base is explicitly given.

We find best fit parameters with one  $\sigma$  errors:

- $k = -1.347 \pm 0.203$
- $Ro_s = 0.155 \pm 0.045$
- $\log(R_s) = -4.436 \pm 0.048$

A comparison of the rotation activity derived in this work to those from

2MASS ID	Mass $M_{\odot}$	$Ro$	$\log(R'_{HK})$	$\log(R'_{HK})_{err}$	$V_{mag}$ mag	$V - K$ mag	prot d	$r_{prot}$
06000351+0242236	0.24	0.020	-4.5475	0.0021	11.31	5.268	1.809	2016ApJ...821
02125458+0000167	0.27	0.048	-4.6345	0.0014	13.58	5.412	4.732	2016ApJ...821
01124752+0154395	0.28	0.026	-4.4729	0.0017	14.009	5.240	2.346	2016ApJ...821
10252645+0512391	0.11	0.000	-4.9707	0.0380	18.11	7.322	0.102	2016ApJ...821
05015746-0656459	0.17	0.873	-5.0049	0.0028	12.2	5.464	88.500	2012AcA....62
06022261-2019447	0.23	1.307	-5.6980	0.0192	13.26	4.886	95.000	This Work
06105288-4324178	0.30	0.705	-5.2507	0.0139	12.28	4.968	53.736	2018AJ....156
09442373-7358382	0.24	0.542	-5.6026	0.0147	15.17	5.795	66.447	2018AJ....156
14211512-0107199	0.24	1.160	-5.5846	0.0125	13.12	5.027	91.426	2018AJ....156
14294291-6240465	0.12	0.394	-5.0053	0.0014	11.13	6.746	83.500	1998AJ....116
16352464-2718533	0.23	1.423	-5.5959	0.0108	14.18	5.182	122.656	2018AJ....156
16570570-0420559	0.24	0.014	-4.3071	0.0014	12.25	5.130	1.212	2012AcA....62
02004725-1021209	0.34	0.188	-4.7907	0.0026	14.118	5.026	14.793	2018AJ....156
18494929-2350101	0.18	0.034	-4.5243	0.0015	10.5	5.130	2.869	2007AcA....57
20035892-0807472	0.33	0.946	-5.6530	0.0077	13.54	5.254	84.991	2018AJ....156
21390081-2409280	0.21	1.152	-6.1949	0.0190	13.45	5.091	94.254	2018AJ....156
23071524-2307533	0.30	0.720	-5.2780	0.0077	13.587	4.849	51.204	2018AJ....156
00094508-4201396	0.30	0.009	-4.3392	0.0018	13.62	5.397	0.859	2018AJ....156
00310412-7201061	0.31	0.906	-5.3879	0.0074	13.69	5.245	80.969	2018AJ....156
01040695-6522272	0.17	0.006	-4.4889	0.0024	13.98	5.448	0.624	2018AJ....156
02014384-1017295	0.19	0.034	-4.5400	0.0022	14.473	5.284	3.152	2018AJ....156
03100305-2341308	0.40	0.028	-4.2336	0.0017	13.502	4.935	2.083	2018AJ....156
03205178-6351524	0.33	1.029	-5.6288	0.0096	13.433	5.238	91.622	2018AJ....156
07401183-4257406	0.15	0.002	-4.3365	0.0022	13.81	6.042	0.307	2018AJ....156
08184619-4806172	0.37	0.021	-4.2834	0.0025	14.37	5.019	1.653	2018AJ....156
08443891-4805218	0.20	1.348	-5.6682	0.0067	13.932	5.370	129.513	2018AJ....156
09342791-2643267	0.19	0.007	-4.3415	0.0025	13.992	5.373	0.694	2018AJ....156
09524176-1536137	0.26	1.342	-5.6319	0.0110	13.43	4.923	99.662	2018AJ....156
11075025-3421003	0.25	0.068	-4.2250	0.0032	15.04	5.633	7.611	2018AJ....156
11575352-2349007	0.39	0.031	-4.2952	0.0026	14.77	5.415	3.067	2018AJ....156
12102834-1310234	0.36	0.435	-4.6892	0.0029	13.83	5.418	42.985	2018AJ....156
12440075-1110302	0.18	0.020	-4.4053	0.0033	14.22	5.546	2.099	2018AJ....156
13442092-2618350	0.35	2.032	-5.9634	0.0253	13.253	4.968	154.885	2018AJ....156
14253413-1148515	0.51	0.301	-4.7641	0.0030	13.512	5.121	25.012	2018AJ....156
14340491-1824106	0.38	0.271	-4.6093	0.0038	14.346	5.638	30.396	2018AJ....156
15154371-0725208	0.38	0.050	-4.6214	0.0023	12.93	5.224	4.379	2018AJ....156
15290145-0612461	0.46	0.095	-4.2015	0.0017	14.011	5.230	8.434	2018AJ....156
16204186-2005139	0.45	0.031	-4.3900	0.0035	13.68	5.261	2.814	2018AJ....156
16475517-6509116	0.17	0.889	-4.8744	0.0045	13.98	5.101	73.142	2018AJ....156
20091824-0113377	0.15	0.010	-4.3772	0.0023	14.47	5.958	1.374	2018AJ....156
20273733-5452592	0.35	1.520	-5.9982	0.0181	13.18	5.259	136.924	2018AJ....156
20444800-1453208	0.49	0.073	-4.4912	0.0023	14.445	5.305	6.715	2018AJ....156
15404341-5101357	0.10	0.318	-5.0062	0.0081	15.26	7.317	93.702	2018AJ....156
22480446-2422075	0.20	0.005	-4.4123	0.0016	12.59	5.384	0.466	2013AJ....146
06393742-2101333	0.26	0.952	-5.2524	0.0069	12.77	5.120	79.152	2018AJ....156
04130560+1514520	0.30	0.019	-4.4775	0.0088	15.881	5.437	1.881	2016ApJ...818
02411510-0432177	0.20	0.004	-4.4272	0.0016	13.79	5.544	0.400	2020ApJ...905
11381671-7721484	0.12	0.958	-5.5015	0.0369	14.78	6.259	153.506	This Work
12384914-3822527	0.15	2.527	-6.0690	0.0156	12.75	5.364	241.913	This Work
13464102-5830117	0.48	1.340	-5.6977	0.0146			65.017	This Work
15165576-0037116	0.31	0.157	-4.0704	0.0024	14.469	5.364	15.028	This Work
19204795-4533283	0.18	1.706	-5.8392	0.0091	12.25	5.405	167.225	This Work
21362532-4401005	0.20	1.886	-5.8978	0.0168	14.14	5.610	207.983	This Work

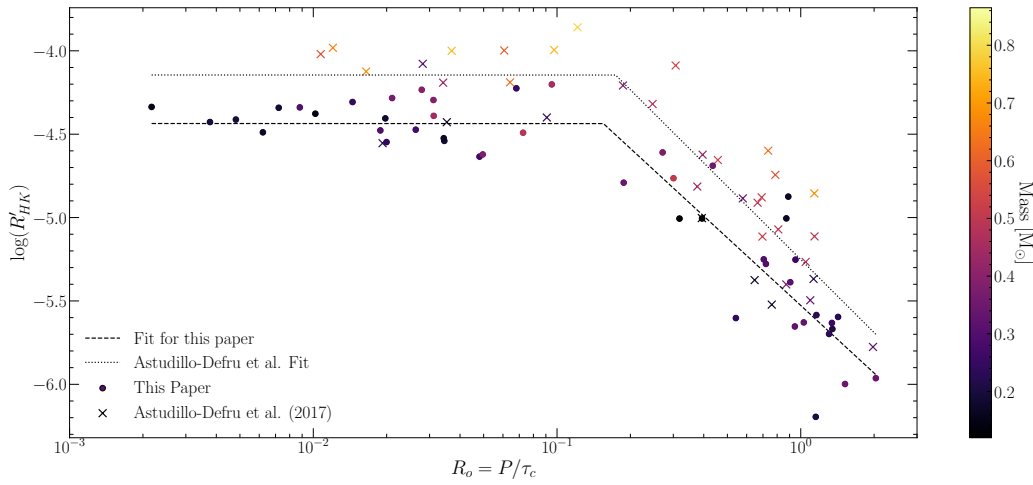


Figure 9.3: Rotation activity relation for both our work and [Astudillo-Defru et al. \(2017\)](#). The dotted line is the best fit to the re-derived rotation-activity relation from [Astudillo-Defru et al. \(2017\)](#). Note that targets from [Astudillo-Defru et al. \(2017\)](#) are systematically higher than targets presented here as a consequence of the range in mass probed by the samples.

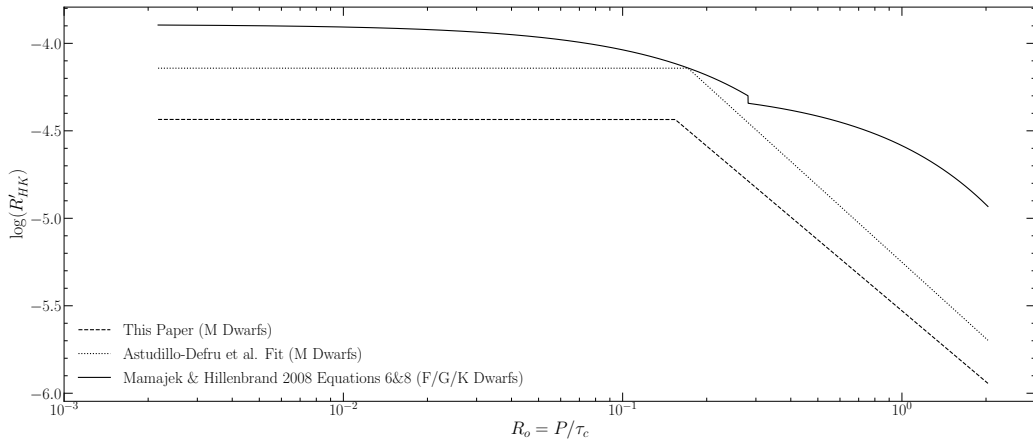


Figure 9.4: Derived rotation-activity curves from this work, [Astudillo-Defru et al. \(2017\)](#) and [Mamajek & Hillenbrand \(2008\)](#). Note both that [Mamajek & Hillenbrand \(2008\)](#) focuses their work on earlier spectral classes and fits the rotation activity relation in linear space.

both [Astudillo-Defru et al. \(2017\)](#) and [Mamajek & Hillenbrand \(2008\)](#) is presented in Figure 9.4. For the 6 targets which do not have measured rotational periods we include an estimate of  $Ro$  and  $p_{rot}$  in the machine readable version of Table 9.1. The convective overturn timescale for one of these 6 targets (2MASS J13464102-5830117) can not be inferred via Equation 9.8 as it lacks a V-K color measurement. Instead, we infer  $\tau_c$  via [Wright et al. \(2018\)](#) Equation 6 (this paper Equation 9.10) using mass. Similar to our manner of inferring  $\tau_c$  via color, when inferring  $\tau_c$  via mass, we adopt the larger of the two antisymmetric errors from [Wright et al. \(2018\)](#).

$$\log_{10}(\tau_c) = 2.33 \pm 0.06 - 1.5 \pm 0.21 (M/M_\odot) + 0.31 \pm 0.17 (M/M_\odot)^2 \quad (9.10)$$

Note that  $R'_{HK}$  for one of six of these targets (2MASS J15165576-0037116) is consistent to within  $1\sigma$  of the saturated value; therefore, the reported  $Ro$  for this target should only be taken as an upper bound. The remaining five targets have measured  $R'_{HK}$  values consistent with the unsaturated regime. Estimated periods are consistent with previous constraints. Of the six stars, two were listed as non-detections in [Newton et al. \(2018\)](#), and the remaining four as uncertain (possible) detections. Of the four classed as uncertain, 2MASS 12384914-3822527 and 2MASS 19204795-4533283 have candidate periods  $> 100$  days and non-detections of H-alpha emission ([Hawley et al., 1996](#)). These two stars and the two non-detections have Ca II H&K activity levels suggesting very long periods. 2MASS 13464102-5830117 has a candidate period of 45 days, and 2MASS 15165576-0037116 of 0.8 days, both consistent with their higher levels of Ca II H&K emission.

As a test of the proposed weak correlation between activity and rotation in the “saturated” regime seen in some works ([Mamajek & Hillenbrand, 2008](#); [Reiners et al., 2014](#); [Lehtinen et al., 2020](#); [Medina et al., 2020](#)) — though not

in others (Wright et al., 2011; Núñez et al., 2015; Newton et al., 2017) — we fit a second model whose power law index is allowed to vary at  $Ro < Ro_s$ . We find a saturated regime power law index of  $-0.052 \pm 0.117$ , consistent with 0 to within  $1\sigma$ . Moreover, all other parameter for this model are consistent to within one  $\sigma$  of the nominal parameters for the model where the index is constrained to 0 below  $Ro = Ro_s$ . We can constrain the slope in the saturated regime to be between -0.363 and 0.259 at the  $3\sigma$  confidence level. Ultimately, we adopt the most standard activity interpretation, a fully-saturated regime at  $Ro < Ro_s$ .

We investigate whether our lack of detection of a slope for  $Ro < Ro_s$  is due to the limited number of observations in that region when compared to other works (e.g. Medina et al., 2020, 93 targets  $Ro < Ro_s$ ) through injection and recovery tests. We inject, fake, rotation-activity measurements into the saturated regime with an a priori slope of -0.13 — the same as in Medina et al.. These fake data are given a standard deviation equal to the standard deviation of our residuals (12%). We preform the same MCMC model fitting to this new data set as was done with the original dataset multiple times, each with progressively more injected data, until we can detect the injected slope to the three sigma confidence level. Ultimately, we need more than 65 data points — 43 more than we observed in the saturated regime — to consistently recover this slope. Therefore, given the spread of our data we cannot detect slopes on the order of what has previously been reported in the literature.

We observe a gap in rotational period over a comparable range to the one presented in Newton et al. (2016) Figure 2. Namely, that M-dwarfs are preferentially observed as either fast or slow rotators, with a seeming lack of stars existing at mid rotational periods. This period gap manifests in the Rossby Number and can be seen in Figure 9.3 as a lack of our targets near to the knee-point in the fit. This period gap likely corresponds to that seen by Browning et al. (2010), who found a paucity of M dwarfs at intermediate activity levels in Ca II H&K and

note the similarity to the Vaughn-Preston gap established in higher mass stars (Vaughan & Preston, 1980). Magaudda et al. (2020) also identify a double-gap in x-ray activity for stars in the unsaturated regime; it is not clear that the gap we see is related. As a consequence of this period gap, there exists a degeneracy in our data between moving the knee-point and allowing the activity level to vary in the saturated regime. In the following, we adopt the model of a fully saturated regime.

We wish to compare our best fit parameters to those derived in Astudillo-Defru et al. (2017); however, the authors of that paper do not fit the knee-point of the rotation-activity relation. They select the canonical value for the rotational period separating the saturated regime from the unsaturated regime ( $P_{rot,s} = 10$  days) and use a fixed convective overturn timescale ( $\tau_c = 70$  days). To make our comparison more meaningful we use the  $P_{rot}$  and  $V - K$  colors presented in Astudillo-Defru et al. (2017) to re-derive  $Ro$  values using  $\tau_c$  (Wright et al., 2018). Doing this for all targets presented in Astudillo-Defru et al. (2017) Table 3 and fitting the same piecewise power law as before, we find best fit parameters of  $Ro_s = 0.17 \pm 0.04$ ,  $\log(R_s) = -4.140 \pm 0.067$ , and  $k = -1.43 \pm 0.21$ . Compared to the best fit parameters for our data,  $Ro_s$  and the unsaturated regime’s index,  $k$ , are consistent to within one sigma, while the saturated value,  $R_s$ , differs.

The mass ranges of our respective samples explain the differences in saturation values between our work and that of Astudillo-Defru et al. (2017). Our work focuses on mid-to-late M-dwarfs and includes no stars above a mass of  $0.5 M_\odot$  (Figure 9.5). The strength of Ca II H&K emission is known to decrease as stellar mass decreases (Schrijver & Rutten, 1987; Rauscher & Marcy, 2006; Houdebine et al., 2017). As Rauscher & Marcy (2006) note, this is the opposite as the trend seen in H-alpha; the latter primarily reflects the increasing length of time that lower M dwarfs remain active and rapidly rotating (West et al., 2015; Newton et al., 2016).

A mass dependence can be seen in Figure 10 in Astudillo-Defru et al. (2017), consistent with expectations from the literature. If we clip the data

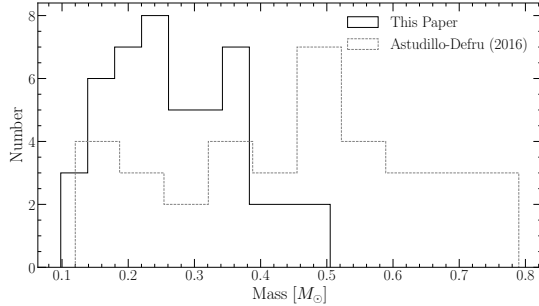


Figure 9.5: Distribution of masses between our sample and the sample presented in [Astudillo-Defru et al. \(2017\)](#). Note how the two studies have approximately the same sample sizes; however, our sample is more tightly concentrated at lower masses \later spectral classes.

from [Astudillo-Defru et al. \(2017\)](#) Table 3 to the same mass range as our data-set ( $M_* < 0.5M_{\odot}$ ) and fit the same function as above, we find that all best fit parameters are consistent to within one sigma between the two data-sets.

We also compare our best fit  $Ro_s$  to both those derived in [Newton et al. \(2017\)](#) using  $H_{\alpha}$  as an activity measure and those derived in ([Wright et al., 2018](#); [Magaudda et al., 2020](#)) using  $L_X/L_{bol}$  as an activity measure. Works using  $L_X/L_{bol}$  identify a similar, yet not consistent to within one sigma result for  $Ro_s$ ; while, the value of  $k$  we find here is consistent between all four works. Therefore, we find similar results not only to other work using the same activity tracer, but also a power-law slope that is consistent with work using different tracers.

## 9.5 Magnetic Activities in M dwarfs Closing Thoughts

In this work we have approximately doubled the number of M-dwarfs with both empirically measured  $R'_{HK}$  with  $M_* < 0.5M_{\odot}$ . This has enabled us to more precisely constrain the rotation-activity relation. This relationship is consistent with other measurements using  $R'_{HK}$ , and  $L_X/L_{bol}$ ; our data does not require a slope in the saturated regime. Finally, we identify a mass dependence in the activity level of the saturated regime, consistent with trends seen in more massive stars in previous works.

## Chapter 10

# Gap Sensitivity to Opacity Source

### 10.1 INTRODUCTION

Due to the initial mass requirements of the molecular clouds which collapse to form stars, star formation is strongly biased towards lower mass, later spectral class stars when compared to higher mass stars. Partly as a result of this bias and partly as a result of their extremely long main-sequence lifetimes, M Dwarfs make up approximately 70 percent of all stars in the galaxy. Moreover, some planet search campaigns have focused on M Dwarfs due to the relative ease of detecting small planets in their habitable zones (e.g. [Nutzman & Charbonneau, 2008](#)). M Dwarfs then represent both a key component of the galactic stellar population as well as the possible set of stars which may host habitable exoplanets. Given this key location M Dwarfs occupy in modern astronomy it is important to have a thorough understanding of their structure and evolution.

[Jao et al. \(2018\)](#) discovered a novel feature in the Gaia Data Release 2 (DR2)  $G_{BP} - G_{RP}$  color-magnitude-diagram. Around  $M_G = 10$  there is an approximately 17 percent decrease in stellar density of the sample of stars [Jao et al. \(2018\)](#) considered. Subsequently, this has become known as either the Jao Gap, or Gaia M Dwarf Gap. Following the initial detection of the Gap in DR2 the Gap has also potentially been observed in 2MASS ([Skrutskie et al., 2006](#); [Jao et al., 2018](#)); however, the significance of this detection is quite weak and it relies on the prior of the Gap's location from Gaia data. Further, the Gap is also present in Gaia Early Data Release 3 (EDR3)

([Jao & Feiden, 2021](#)). These EDR3 and 2MASS data sets then indicate that this feature is not a bias inherent to DR2.

The Gap is generally attributed to convective instabilities in the cores of stars straddling the fully convective transition mass (0.3 - 0.35 M<sub>⊕</sub>) ([Baraffe & Chabrier, 2018](#)). These instabilities interrupt the normal, slow, main sequence luminosity evolution of a star and result in luminosities lower than expected from the main sequence mass-luminosity relation ([Jao & Feiden, 2020](#)).

The Jao Gap, inherently a feature of M Dwarf populations, provides an enticing and unique view into the interior physics of these stars ([Feiden et al., 2021](#)). This is especially important as, unlike more massive stars, M Dwarf seismology is infeasible due to the short periods and extremely small magnitudes which both radial and low-order low-degree non-radial seismic waves are predicted to have in such low mass stars ([Rodríguez-López, 2019](#)). The Jao Gap therefore provides one of the only current methods to probe the interior physics of M Dwarfs.

Despite the early success of modeling the Gap some issues remain. [Jao & Feiden \(2020, 2021\)](#) identify that the Gap has a wedge shape which has not been successfully reproduced by any current modeling efforts and which implies a somewhat unusual population composition of young, metal-poor stars. Further, [Jao & Feiden \(2020\)](#) identify substructure, an additional over density of stars, directly below the Gap, again a feature not yet fully captured by current models.

All currently published models of the Jao Gap make use of OPAL high temperature radiative opacities. Here we investigate the effect of using the more up-to-date OPLIB high temperature radiative opacities and whether these opacity tables bring models more in line with observations. In Section 10.2 we provide an overview of the physics believed to result in the Jao Gap, in Section 10.3 we review the differences between OPAL and OPLIB and describe how we update DSEP to use OPLIB opacity tables. Section 11.3 walks through the stellar evolution and population synthesis modeling we perform. Finally, in Section 11.2 we present our findings.

## 10.2 Jao Gap

A theoretical explanation for the Jao Gap (Figure 10.1) comes from [van Saders & Pinsonneault \(2012\)](#), who propose that in a star directly above the transition mass, due to asymmetric production and destruction of  ${}^3\text{He}$  during the proton-proton I chain (ppI), periodic luminosity variations can be induced. This process is known as convective-kissing instability. Very shortly after the zero-age main sequence such a star will briefly develop a radiative core; however, as the core temperature exceeds  $7 \times 10^6$  K, enough energy will be produced by the ppI chain that the core once again becomes convective. At this point the star exists with both a convective core and envelope, in addition to a thin, radiative layer separating the two. Subsequently, asymmetries in ppI affect the evolution of the star's convective core.

While kissing instability has been the most widely adopted model to explain the existence of the Jao Gap, slightly different mechanisms have also been proposed. [MacDonald & Gizis \(2018\)](#) make use of a fully implicit stellar evolution suite which treats convective mixing as a diffusive property. [MacDonald & Gizis](#) treat convective mixing this way in order to account for a core deuterium concentration gradient proposed by [Baraffe et al. \(1997\)](#). Under this treatment the instability results only in a single mixing event — as opposed to periodic mixing events. Single mixing events may be more in line with observations (see section 11.2 for more details on how periodic mixings can effect a synthetic population) where there is only well documented evidence of a single gap. However, recent work by [Jao & Feiden \(2021\)](#) which identify an second under density of stars below the canonical gap, does leave the door open for the periodic mixing events.

The proton-proton I chain constitutes three reactions

1.  $p + p \longrightarrow d + e^+ + \nu_e$
2.  $p + d \longrightarrow {}^3\text{He} + \gamma$
3.  ${}^3\text{He} + {}^3\text{He} \longrightarrow {}^3\text{He} + 2p$

Initially, reaction 3 of ppI consumes  ${}^3\text{He}$  at a slower rate than it is produced by reac-

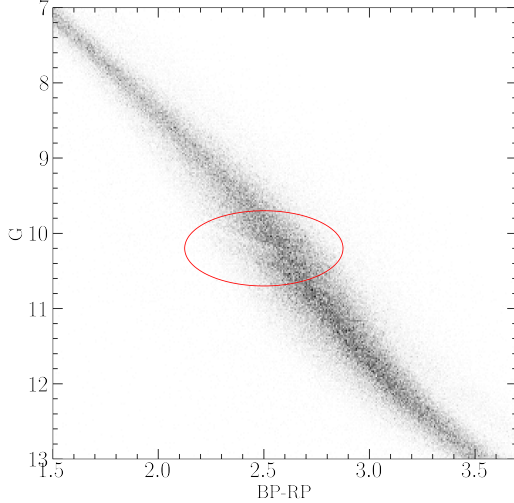


Figure 10.1: The Jao Gap (circled) seen in the Gaia Catalogue of Nearby Stars ([Gaia Collaboration et al., 2021](#)).

tion 2 and as a result, the core  $^3\text{He}$  abundance and consequently the rate of reaction 3, increases with time. The core convective zone expands as more of the star becomes unstable to convection. This expansion continues until the core connects with the convective envelope. At this point convective mixing can transport material throughout the entire star and the high concentration of  $^3\text{He}$  rapidly diffuses outward, away from the core, decreasing energy generation as reaction 3 slows down. Ultimately, this leads to the convective region around the core pulling back away from the convective envelope, leaving in place the radiative transition zone, at which point  $^3\text{He}$  concentrations grow in the core until it once again expands to meet the envelope. These periodic mixing events will continue until  $^3\text{He}$  concentrations throughout the star reach an equilibrium ultimately resulting in a fully convective star. Figure 10.2 traces the evolution of a characteristic star within the Jao Gap’s mass range.

### 10.2.1 Efforts to Model the Gap

Since the identification of the Gap, stellar modeling has been conducted to better constrain its location, effects, and exact cause. Both [Mansfield & Kroupa \(2021\)](#) and [Feiden et al. \(2021\)](#) identify that the Gap’s mass location is correlated with model metallicity — the mass-luminosity discontinuity in lower metallicity models being at

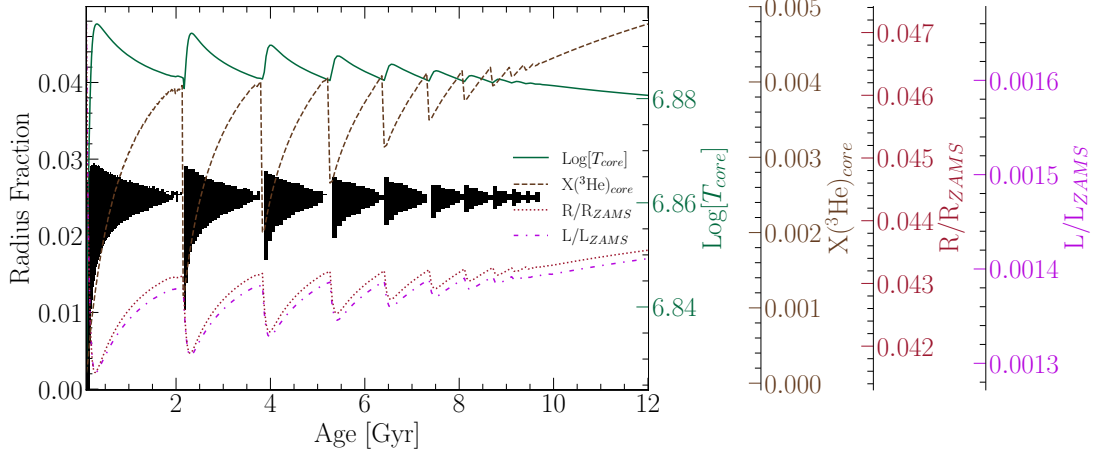


Figure 10.2: Diagram for a characteristic stellar model of  $0.35625 M_{\odot}$  which is within the Jao Gap’s mass range. The black shaded regions denote whether, at a particular model age, a radial shell within the model is radiative (with white meaning convective). The lines trace the models core temperature, core  ${}^3\text{He}$  mass fraction, fractional luminosity wrt. the zero age main sequence and fractional radius wrt. the zero age main sequence.

a commensurately lower mass. [Feiden et al. \(2021\)](#) suggests this dependence is due to the steep relation of the radiative temperature gradient,  $\nabla_{rad}$ , on temperature and, in turn, on stellar mass.

$$\nabla_{rad} \propto \frac{L\kappa}{T^4} \quad (10.1)$$

As metallicity decreases so does opacity, which, by Equation 10.1, dramatically lowers the temperature at which radiation will dominate energy transport ([Chabrier & Baraffe, 1997](#)). Since main sequence stars are virialized the core temperature is proportional to the core density and total mass. Therefore, if the core temperature where convective-kissing instability is expected decreases with metallicity, so too will the mass of stars which experience such instabilities.

The strong opacity dependence of the Jao Gap begs the question: what is the effect of different opacity calculations on Gap properties. As we can see above, changing opacity should affect the Gap’s location in the mass-luminosity relation and therefore in a color-magnitude diagram. Moreover, current models of the Gap have yet to locate

it precisely in the CMD ([Feiden et al., 2021](#)) with an approximate 0.16 G-magnitude difference between the observed and modeled Gaps. Opacity provides one, as yet unexplored, parameter which has the potential to resolve these discrepancies.

### 10.3 Updated Opacities

Multiple groups have released high-temperature opacities including, the Opacity Project (OP [Seaton et al., 1994](#)), Laurence Livermore National Labs OPAL opacity tables ([Iglesias & Rogers, 1996](#)), and Los Alamos National Labs OPLIB opacity tables ([Colgan et al., 2016](#)). OPAL high-temperature radiative opacity tables in particular are very widely used by current generation isochrone grids (e.g. Dartmouth, MIST, & StarEvol, [Dotter et al., 2008](#); [Choi et al., 2016](#); [Amard et al., 2019](#)). OPLIB opacity tables ([Colgan et al., 2016](#)) are not widely used but include the most up-to-date plasma modeling.

While the overall effect on the CMD of using OPLIB compared to OPAL tables is small, the strong theoretical opacity dependence of the Jao Gap raises the potential for these small effects to measurably shift the Gap’s location. We update DSEP to use high temperature opacity tables based on measurements from Los Alamos national Labs T-1 group (OPLIB, [Colgan et al., 2016](#)). The OPLIB tables are created with ATOMIC ([Magee et al., 2004](#); [Hakel et al., 2006](#); [Fontes et al., 2015](#)), a modern LTE and non-LTE opacity and plasma modeling code. These updated tables were initially created in order to incorporate the most up to date plasma physics at the time ([Bahcall et al., 2005](#)).

OPLIB tables include monochromatic Rosseland mean opacities — composed from bound-bound, bound-free, free-free, and scattering opacities — for elements hydrogen through zinc over temperatures 0.5eV to 100 keV (5802 K –  $1.16 \times 10^9$  K) and for mass densities from approximately  $10^{-8}$  g cm $^{-3}$  up to approximately  $10^4$  g cm $^{-3}$  (though the exact mass density range varies as a function of temperature).

DSEP ramps the [Ferguson et al. \(2005\)](#) low temperature opacities to high temperature opacities tables between  $10^{4.3}$  K and  $10^{4.5}$  K; therefore, only differences between high-temperature opacity sources above  $10^{4.3}$  K can effect model evolution.

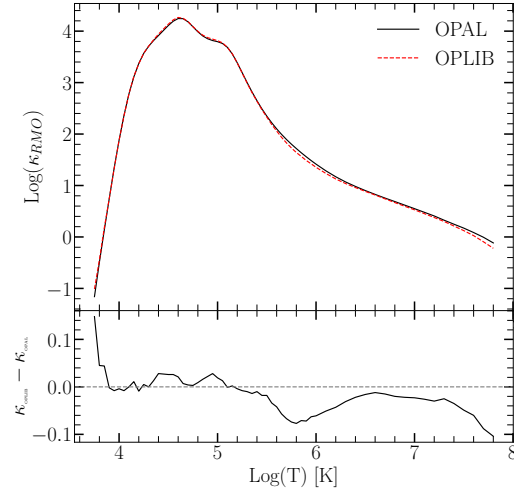


Figure 10.3: Rosseland mean opacity with the GS98 solar composition for both OPAL opacities and OPLIB opacities (top). Residuals between OPLIB opacities and OPAL opacities (bottom). These opacities are plotted at  $\log_{10}(R) = -0.5$ ,  $X = 0.7$ , and  $Z = 0.02$ .  $\log_{10}(R) = -0.5$  approximates much of the interior a  $0.35 M_\odot$  model. Note how the OPLIB opacities are systematically lower than the OPAL opacities for temperatures above  $10^{5.2}$  K.

When comparing OPAL and OPLIB opacity tables (Figure 10.3) we find OPLIB opacities are systematically lower than OPAL opacities for temperatures above  $10^5$  K. Between  $10^{4.3}$  and  $10^5$  K OPLIB opacities are larger than OPAL opacities. These generally lower opacities will decrease the radiative temperature gradient throughout much of the radius of a model.

### 10.3.1 Table Querying and Conversion

The high-temperature opacity tables used by DSEP and most other stellar evolution programs give Rosseland-mean opacity,  $\kappa_R$ , along three dimensions: temperature, a density proxy  $R$  (Equation 10.2;  $T_6 = T \times 10^{-6}$ ,  $\rho$  is the mass density), and composition.

$$R = \frac{\rho}{T_6^3} \quad (10.2)$$

OPLIB tables may be queried from a web interface<sup>1</sup>; however, OPLIB opacities are

---

<sup>1</sup><https://aphysics2.lanl.gov/apps/>

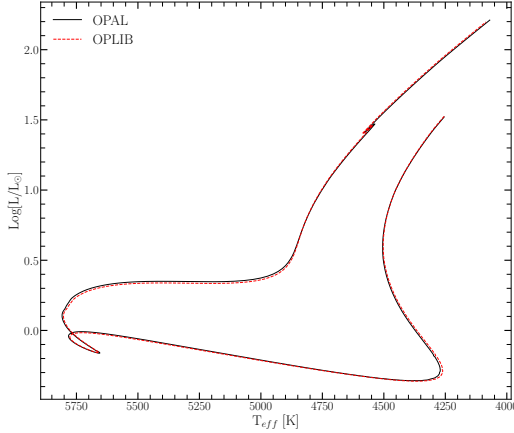


Figure 10.4: HR Diagram for the two SCSMs, OPAL and OPLIB. OPLIB is shown as a red dashed line.

parametrized using mass-density and temperature instead of  $R$  and temperature. It is most efficient for us to convert these tables to the OPAL format instead of modifying DSEP to use the OPLIB format directly. In order to generate many tables easily and quickly we develop a web scraper (pyTOPSScrape, ?) which can automatically retrieve all the tables needed to build an opacity table in the OPAL format. pyTOPSScrape<sup>2</sup> has been released under the permissive MIT license with the consent of the Los Alamos T-1 group. For a detailed discussion of how the web scraper works and how OPLIB tables are transformed into a format DSEP can use see Appendices 10.4 & 10.5.

### 10.3.2 Solar Calibrated Stellar Models

In order to validate the OPLIB opacities, we generate a solar calibrated stellar model (SCSM) using these new tables. We first manually calibrate the surface Z/X abundance to within one part in 100 of the solar value (Grevesse & Sauval, 1998, Z/X=0.23). Subsequently, we allow both the convective mixing length parameter,  $\alpha_{ML}$ , and the initial Hydrogen mass fraction,  $X$ , to vary simultaneously, minimizing the difference, to within one part in  $10^5$ , between resultant models' final radius and luminosity to those of the sun. Finally, we confirm that the model's surface Z/X abundance is still within one part in 100 of the solar value.

Solar calibrated stellar models evolved using GS98 OPAL and OPLIB opacity

<sup>2</sup><https://github.com/tboudreux/pytopsscrape>

Model	$X$	$\alpha_{ML}$
OPAL	0.7066	1.9333
OPLIB	0.7107	1.9629

Table 10.1: Optimized parameters for SCSMs evolved using OPAL and OPLIB high temperature opacity tables.

tables (Figure 10.4) differ  $\sim 0.5\%$  in the SCSM hydrogen mass fractions and  $\sim 1.5\%$  in the SCSM convective mixing length parameters (Table 10.1). While the two evolutionary tracks are very similar, note that the OPLIB SCSM’s luminosity is systematically lower past the solar age. While at the solar age the OPLIB SCSM luminosity is effectively the same as the OPAL SCSM. This luminosity difference between OPAL and OPLIB based models is not inconsistent with expectations given the more shallow radiative temperature gradient resulting from the lower OPLIB opacities

## 10.4 pyTOPSScrape

`pyTOPSScrape` provides an easy to use command line and python interface for the OPLIB opacity tables accessed through the TOPS web form. Extensive documentation of both the command line and programmatic interfaces is linked in the version controlled repository. However, here we provide a brief, illustrative, example of potential use.

Assuming `pyTOPSScrape` has been installed and given some working directory which contains a file describing a base composition (“comp.dat”) and another file containing a list of rescalings of that base composition (“rescalings.dat”) (both of these file formats are described in detail in the documentation), one can query OPLIB opacity tables and convert them to a form mimicking that of type 1 OPAL high temperature opacity tables using the following shell command.

```
$ generateTOPStables comp.dat rescalings.dat -d ./TOPSCache -o out.opac -j 20
```

For further examples of `pyTOPSScrape` please visit the repository.

## 10.5 Interpolating $\rho \rightarrow R$

OPLIB parameterizes  $\kappa_R$  as a function of mass density, temperature in keV, and composition. Type 1 OPAL high temperature opacity tables, which DSEP and many other stellar evolution programs use, instead parameterizes opacity as a function of temperature in Kelvin,  $R$  (Equation 10.3), and composition. The conversion from temperature in keV to Kelvin is trivial (Equation 10.4).

$$R = \frac{\rho}{T_6^3} \quad (10.3)$$

$$T_K = T_{keV} * 11604525.0061657 \quad (10.4)$$

However, the conversion from mass density to  $R$  is more involved. Because  $R$  is coupled with both mass density and temperature there is no way to directly convert tabulated values of opacity reported in the OPLIB tables to their equivalents in  $R$  space. The TOPS webform does allow for a density range to be specified at a specific temperature, which allows for  $R$  values to be directly specified. However, issuing a query to the TOPS webform for not just every composition in a Type 1 OPAL high temperature opacity table but also every temperature for every composition will increase the number of calls to the webform by a factor of 70. Therefore, instead of directly specifying  $R$  through the density range we choose to query tables over a broad temperature and density range and then rotate these tables, interpolating  $\kappa_R(\rho, T_{eff}) \rightarrow \kappa_R(R, T_{eff})$ .

To perform this rotation we use the `interp2d` function within `scipy`'s `interpolate` (?) module to construct a cubic bivariate B-spline ([DIERCKX, 1981](#)) interpolating function  $s$ , with a smoothing factor of 0, representing the surface  $\kappa_R(\rho, T_{eff})$ . For each  $R^i$  and  $T_{eff}^j$  reported in type 1 OPAL tables, we evaluate Equation 10.3 to find  $\rho^{ij} = \rho(T_{eff}^j, R^i)$ . Opacities in  $T_{eff}$ ,  $R$  space are then inferred as  $\kappa_R^{ij}(R^i, T_{eff}^j) = s(\rho^{ij}, T_{eff}^j)$ .

As first-order validation of this interpolation scheme we can perform a similar

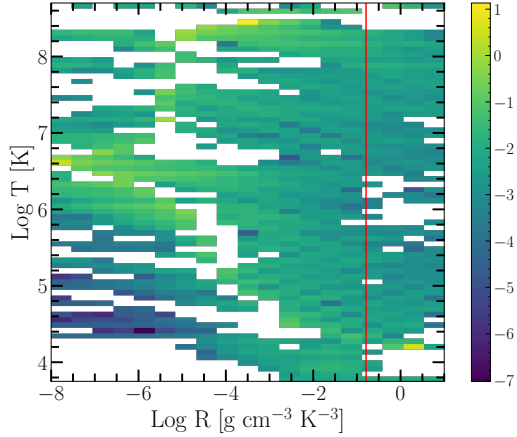


Figure 10.5: Log Fractional Difference between opacities in  $\kappa_R(\rho, T_{eff})$  space directly queried from the OPLIB web-form and those which have been interpolated into  $\log(R)$  space and back. Note that, due to the temperature grid of type 1 OPAL tables not aligning perfectly with the temperature grid OPLIB uses there may be edge effects where the interpolation is poorly constrained. The red line corresponds to  $\log(R) = -0.79$  where much of a stellar model’s radius exists.

interpolation in the opposite direction, rotating the tables back to  $\kappa_R(\rho, T_{eff})$  and then comparing the initial, “raw”, opacities to those which have gone through the interpolations process. Figure 10.5 shows the fractional difference between the raw opacities and a set which have gone through this double interpolation. The red line denotes  $\log(R) = -0.79$  where models near the Jao Gap mass range will tend to sit for much of their radius. Along the  $\log(R) = -0.79$  line the mean fractional difference is  $\langle \delta \rangle = 0.005$  with an uncertainty of  $\sigma_{\langle \delta \rangle} = 0.013$ . One point of note is that, because the initial rotation into  $\log(R)$  space also reduces the domain of the opacity function, interpolation-edge effects which we avoid initially by extending the domain past what type 1 OPAL tables include cannot be avoided when interpolating back into  $\rho$  space.

## 10.6 Modeling

In order to model the Jao Gap we evolve two extremely finely sampled mass grids of models. One of these grids uses the OPAL high-temperature opacity tables while the other uses the OPLIB tables (Figure 10.6). Each grid evolves a model every  $0.00025 M_\odot$  from  $0.2$  to  $0.4 M_\odot$  and every  $0.005 M_\odot$  from  $0.4$  to  $0.8 M_\odot$ . All models in both grids use a GS98 solar composition, the (1, 101, 0) FreeEOS (version 2.7)

configuration, and 1000 year old pre-main sequence polytropic models, with polytropic index 1.5, as their initial conditions. We include gravitational settling in our models where elements are grouped together. Finally, we set a maximum allowed timestep of 50 million years to assure that we fully resolve the build of core  $^3\text{He}$  in gap stars.

Despite the alternative view of convection provided by [MacDonald & Gizis \(2018\)](#) discussed in Section 10.2, given that the mixing timescales in these low mass stars are so short (between  $10^7$ s and  $10^8$ s per [Jermyn et al., 2022](#), Figure 2 & Equation 39, which present the averaged velocity over the convection zone) instantaneous mixing is a valid approximation. Moreover, one principal motivation for a diffusive model of convective mixing has been to account for a deuterium concentration gradient which [Chabrier & Baraffe \(1997\)](#) identify will develop when the deuterium lifetime against proton capture is significantly shorter than the mixing timescale. However, the treatment of energy generation used by DSEP ([Bahcall et al., 2001](#)) avoids this issue by computing both the equilibrium deuterium abundance and luminosity of each shell individually, implicitly accounting for the overall luminosity discrepancy identified by [Chabrier & Baraffe](#).

Because in this work we are just interested in the location shift of the Gap as the opacity source varies, we do not model variations in composition. [Mansfield & Kroupa \(2021\)](#); [Jao & Feiden \(2020\)](#); [Feiden et al. \(2021\)](#) all look at the effect composition has on Jao Gap location. They find that as population metallicity increases so too does the mass range and consequently the magnitude of the Gap. From an extremely low metallicity population ( $Z=0.001$ ) to a population with a more solar like metallicity this shift in mass range can be up to  $0.05 M_\odot$  ([Mansfield & Kroupa, 2021](#)).

### 10.6.1 Population Synthesis

In order to compare the Gap to observations we use in house population synthesis code. We empirically calibrate the relation between G, BP, and RP magnitudes and their uncertainties along with the parallax/G magnitude uncertainty relation using the Gaia Catalogue of Nearby Stars (GCNS, [Gaia Collaboration et al., 2021](#)) and Equations 10.5 & 10.6.  $M_g$  is the Gaia G magnitude while  $M_i$  is the magnitude

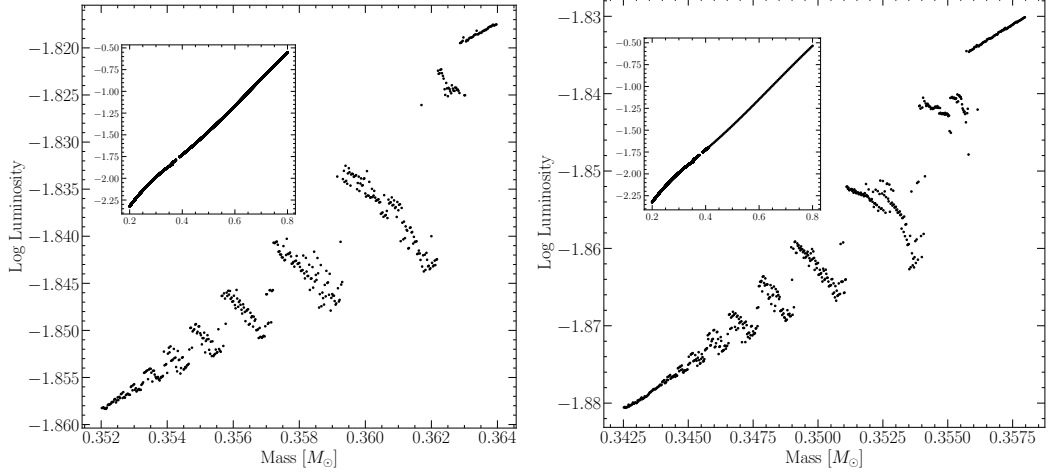


Figure 10.6: Mass-luminosity relation at 7 Gyrs for models evolved using OPAL opacity tables (top) and those evolved using OPLIB opacity tables (bottom). Note the lower mass range of the OPLIB Gap.

in the  $i^{\text{th}}$  band, G, BP, or RP. The coefficients  $a$ ,  $b$ , and  $c$  determined using a non-linear least squares fitting routine. Equation 10.5 then models the relation between G magnitude and parallax uncertainty while Equation 10.6 models the relation between each magnitude and its uncertainty.

$$\sigma_{plx}(M_g) = ae^{bM_g} + c \quad (10.5)$$

$$\sigma_i(M_i) = ae^{M_i - b} + c \quad (10.6)$$

The full series of steps in our population synthesis code are:

1. Sample from a [Sollima \(2019\)](#) ( $0.25M_{\odot} < M < 1M_{\odot}$ ,  $\alpha = -1.34 \pm 0.07$ ) IMF to determine synthetic star mass.
2. Find the closest model above and below the synthetic star, linearly interpolate these models'  $T_{\text{eff}}$ ,  $\log(g)$ , and  $\log(L)$  to those at the synthetic star mass.
3. Convert synthetic star  $g$ ,  $T_{\text{eff}}$ , and  $\log(L)$  to Gaia G, BP, and RP magnitudes using the Gaia (E)DR3 bolometric corrections ([Creevey et al., 2022](#)) along with code obtained thorough personal communication with Aaron Dotter ([Choi et al.,](#)

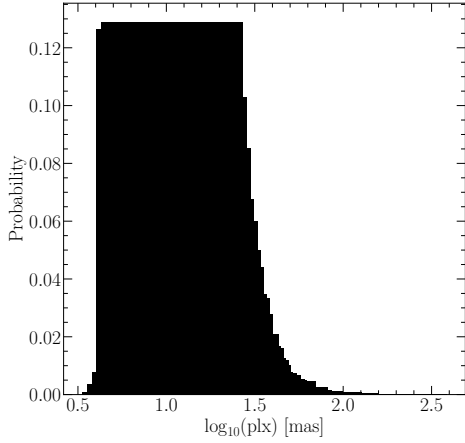


Figure 10.7: Probability distribution sampled when assigning true parallaxes to synthetic stars. This distribution is built from the GCNS and includes all stars with BP-RP colors between 2.3 and 2.9, the same color range of the Jao Gap.

2016).

4. Sample from the GCNS parallax distribution (Figure 10.7), limited to stars within the BP-RP color range of 2.3 – 2.9, to assign synthetic star a “true” parallax.
5. Use the true parallax to find an apparent magnitude for each filter.
6. Evaluate the empirical calibration given in Equation 10.5 to find an associated parallax uncertainty. Then sample from a normal distribution with a standard deviation equal to that uncertainty to adjust the true parallax resulting in an “observed” parallax.
7. Use the “observed” parallax and the apparent magnitude to find an “observed” magnitude.
8. Fit the empirical calibration given in Equation 10.6 to the GCNS and evaluate it to give a magnitude uncertainty scale in each band.
9. Adjust each magnitude by an amount sampled from a normal distribution with a standard deviation of the magnitude uncertainty scale found in the previous step.

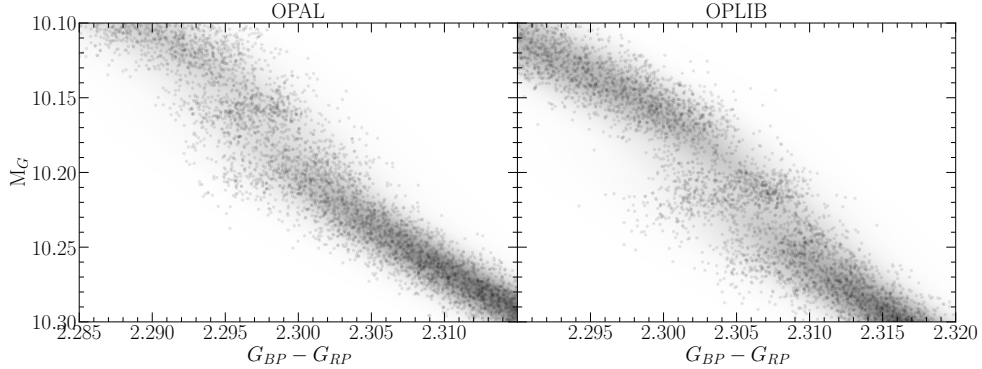


Figure 10.8: Population synthesis results for models evolved with OPAL (left) and models evolved with OPLIB (right). A Gaussian kernel-density estimate has been overlaid to better highlight the density variations.

This method then incorporates both photometric and astrometric uncertainties into our population synthesis. An example 7 Gyr old synthetic populations using OPAL and OPLIB opacities are presented in Figure 10.8.

### 10.6.2 Mixing Length Dependence

In order to test the sensitivity of Gap properties to mixing length we evolve three separate sets OPLIB of models. The first uses a GS98 solar calibrated mixing length, the second uses a mixing length of 1.5, and the third uses a mixing length of 1.0.

We find a clear inverse correlation between mixing length parameter used and the magnitude of the Jao Gap Figures 10.9 & 10.10 ( $\mu_G \propto -1.5\alpha_{ML}$ , where  $\mu_G$  is the mean magnitude of the Gap). This is somewhat surprising given the long established view that the mixing length parameter is of little relevance in fully convective stars (Baraffe et al., 1997). We find an approximate 0.3 magnitude shift in both the color and magnitude comparing a solar calibrated mixing length to a mixing length of 1.5, despite only a 16K difference in effective temperature at 7Gyr between two 0.3 solar mass models. The slight temperature differences between these models are attributable to the steeper adiabatic temperature gradients just below the atmosphere in the solar calibrated mixing length model compared to the  $\alpha_{ML} = 1.5$  model ( $\nabla_{ad,solar} - \nabla_{ad,1.5} \approx 0.05$ ). Despite this relatively small temperature variance, the large magnitude difference is expected due to the extreme sensitivity of the bolo-

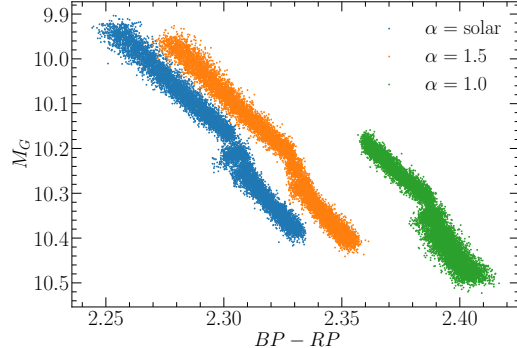


Figure 10.9: CMD showing OPLIB populations (from left to right) A, B, and C.

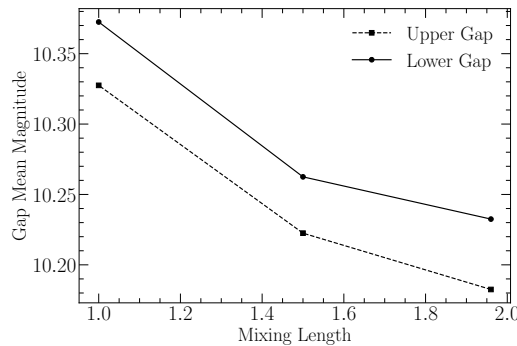


Figure 10.10: Location of the two identified paucities of stars in OPLIB synthetic populations as a function of the mixing length used.

metric corrections on effective temperature at these low temperatures. The mixing length then provides a free parameter which may be used to shift the gap location in order to better match observations without having a major impact on the effective temperature of models. Moreover, recent work indicates that using a solar calibrated mixing length is not appropriate for all stars (e.g. [Trampedach et al., 2014](#); [Joyce & Chaboyer, 2018](#)).

Given the variability of gap location with mixing length, it is possible that a better fit to the gap location may be achieved through adjustment of the convective mixing length parameter. However, calibrations of the mixing length for stars other than the sun have focused on stars with effective temperature at or above that of the sun and there are no current calibrations of the mixing length parameter for M dwarfs. Moreover, there are additional uncertainties when comparing the predicted gap location to the measured gap location, such as those in the conversion from effective tempera-

ture, surface gravity, and luminosity to color, which must be considered if the mixing length is to be used as a gap location free parameter. Given the dangers of freely adjustable parameters and the lack of an a priori expectation for what the convective mixing parameter should be for the population of M Dwarfs in the Gaia DR2 and EDR3 CMD any attempt to use the Jao Gap magnitude to calibrate a mixing length value must be done with caution, and take into account the other uncertainties in the stellar models which could affect the Jao Gap magnitude.

## 10.7 Results

We quantify the Jao Gap location along the magnitude (Table 10.2) axis by sub-sampling our synthetic populations, finding the linear number density along the magnitude axis of each sub-sample, averaging these linear number densities, and extracting any peaks above a prominence threshold of 0.1 as potential magnitudes of the Jao Gap (Figure 10.11). Gap widths are measured at 50% the height of the peak prominence. We use the python package `scipy` (?) to both identify peaks and measure their widths.

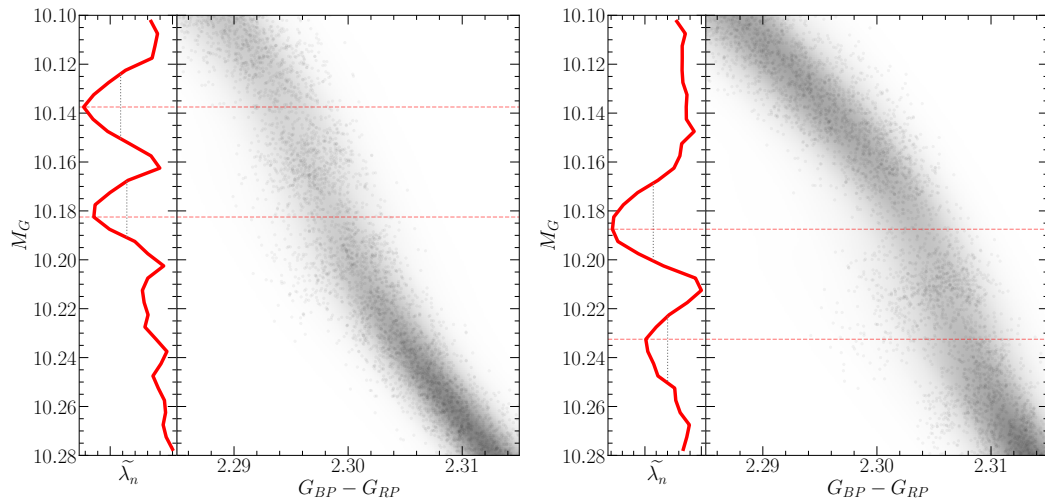


Figure 10.11: (right panels) OPAL (left) and OPLIB (right) synthetic populations. (left panels) Normalized linear number density along the magnitude axis. A dashed line has been extended from the peak through both panels to make clear where the identified Jao Gap location is wrt. to the population.

In both OPAL and OPLIB synthetic populations our Gap identification method

Model	Location	Prominence	Width
OPAL 1	10.138	0.593	0.027
OPAL 2	10.183	0.529	0.023
OPLIB 1	10.188	0.724	0.032
OPLIB 2	10.233	0.386	0.027

Table 10.2: Locations identified as potential Gaps.

finds two gaps above the prominence threshold. The identification of more than one gap is not inconsistent with the mass-luminosity relation seen in the grids we evolve. As noise is injected into a synthetic population smaller features will be smeared out while larger ones will tend to persist. The mass-luminosity relations shown in Figure 10.6 make it clear that there are: (1), multiple gaps due to stars of different masses undergoing convective mixing events at different ages, and (2), the gaps decrease in width moving to lower masses / redder. Therefore, the multiple gaps we identify are attributable to the two bluest gaps being wide enough to not smear out with noise. In fact, if we lower the prominence threshold just slightly from 0.1 to 0.09 we detect a third gap in both the OPAL and OPLIB datasets where one would be expected.

Previous modeling efforts (e.g. [Feiden et al., 2021](#)) have not identified multiple gaps. This is likely due to two reasons: (1), previous studies have allowed metallicity to vary across their model grids, further smearing the gaps out, and (2), previous studies have used more coarse underlying mass grids, obscuring features smaller than their mass step. While this dual-gap structure has not been seen in models before, a more complex gap structure is not totally unprecedented as [Jao & Feiden \(2021\)](#) identifies an additional under-dense region below the primary gap in EDR3 data. As part of a follow up series of papers, we are conducting further work to incorporate metallicity variations while still using the finer mass sampling presented here.

The mean gap location of the OPLIB population is at a fainter magnitude than the mean gap location of the OPAL population. Consequently, in the OPLIB sample the convective mixing events which drive the kissing instability begin happening at lower masses (i.e. the convective transition mass decreases). A lower mass range will naturally result in a fainter mean gap magnitude.

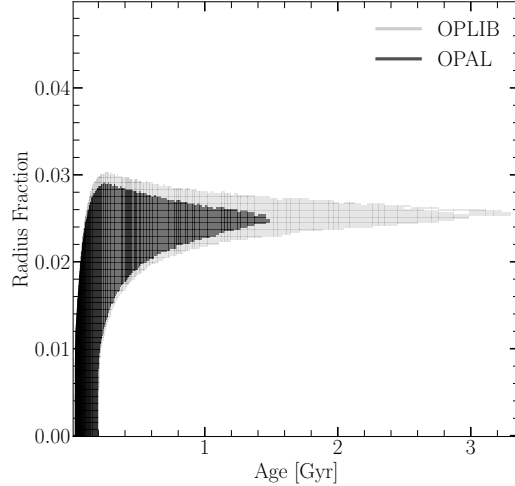


Figure 10.12: Portions of  $0.3526 M_{\odot}$  OPAL and OPLIB stellar models showing the interior shells which are radiative (black region). Note that for clarity only one convective mixing event from each model is shown. Note how the radiative zone in the OPLIB model is larger.

Mixing events at lower masses in OPLIB models are attributable to the radially thicker, at the same mass, radiative zones (Figure 10.12). This thicker radiative zone will take more time to break down and is characteristic of OPLIB models as of a result of their slightly lower opacities. A lower opacity fluid will have a more shallow radiative temperature gradient than a higher opacity fluid; however, as the adiabatic temperature gradient remains essentially unchanged as a function of radius, a larger interior radius of the model will remain unstable to radiation. This thicker radiative zone will increase the time it takes the core convective zone to meet up with convective envelope meaning that lower mass models can sustain a radiative zone for longer than they could otherwise; thus; lower opacities push the convective transition mass down. We can additionally see this longer lived radiative zone in the core  $^3\text{He}$  mass fraction, in which OPLIB models reach much higher concentrations — at approximately the same growth rate — for the same mass as OPAL models do (Figure 10.13).

The most precise published Gap location comes from [Jao & Feiden \(2020\)](#) who use EDR3 to locate the Gap at  $M_G \sim 10.3$ , we identify the Gap at a similar location in the GCNS data. The Gap in populations evolved using OPLIB tables is closer to this measurement than it is in populations evolved using OPAL tables (Table 10.2).

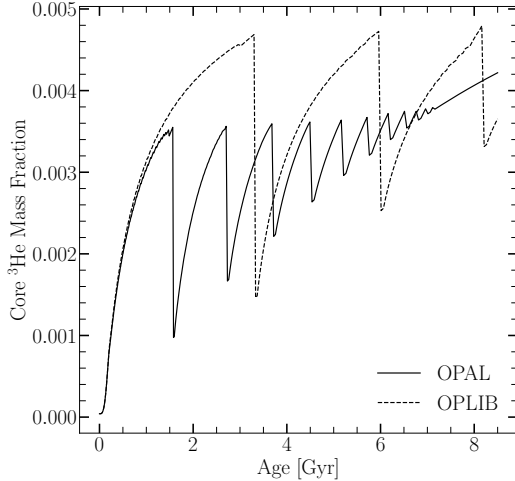


Figure 10.13: Core  ${}^3\text{He}$  mass fraction for  $0.3526 M_{\odot}$  models evolved with OPAL and OPLIB (within the Jao Gap’s mass range for both). Note how the OPLIB model’s core  ${}^3\text{He}$  mass fraction grows at approximately the same rate as the OPAL model’s but continues uninterrupted for longer.

It should be noted that the exact location of the observed Gap is poorly captured by a single value as the Gap visibly compresses across the width of the main-sequence, wider on the blue edge and narrower on the red edge such that the observed Gap has downward facing a wedge shape (Figure 10.1). This wedge shape is not successfully reproduced by either any current models or the modeling we perform here. We elect then to specify the Gap location where this wedge is at its narrowest, on the red edge of the main sequence.

The Gaps identified in our modeling have widths of approximately 0.03 magnitudes, while the shift from OPAL to OPLIB opacities is 0.05 magnitudes. With the prior that the Gaps clearly shift before noise is injected we know that this shift is real. However, the shift magnitude and Gap width are of approximately the same size in our synthetic populations. Moreover, Feiden et al. (2021) identify that the shift in the modeled Gap mass from  $[\text{Fe}/\text{H}] = 0$  to  $[\text{Fe}/\text{H}] = +0.5$  as  $0.04M_{\odot}$ , whereas we only see an approximate  $0.01 M_{\odot}$  shift between OPAL and OPLIB models. Therefore, the Gap location will likely not provide a usable constraint on the opacity source.

# Chapter 11

## Jao Gap connection to Magnetism

### 11.1 INTRODUCTION

Due to the initial mass requirements of the molecular clouds which collapse to form stars, star formation is strongly biased towards lower mass, later spectral class stars when compared to higher mass stars. Partly as a result of this bias and partly as a result of their extremely long main-sequence lifetimes, M Dwarfs make up approximately 70 percent of all stars in the galaxy. Moreover, some planet search campaigns have focused on M Dwarfs due to the relative ease of detecting small planets in their habitable zones (e.g. [Nutzman & Charbonneau, 2008](#)). M Dwarfs then represent both a key component of the galactic stellar population as well as the possible set of stars which may host habitable exoplanets. Given this key location M Dwarfs occupy in modern astronomy it is important to have a thorough understanding of their structure and evolution.

[Jao et al. \(2018\)](#) discovered a novel feature in the Gaia Data Release 2 (DR2)  $G_{BP} - G_{RP}$  color-magnitude-diagram. Around  $M_G = 10$  there is an approximately 17 percent decrease in stellar density of the sample of stars [Jao et al. \(2018\)](#) considered. Subsequently, this has become known as either the Jao Gap, or Gaia M Dwarf Gap. Following the initial detection of the Gap in DR2 the Gap has also potentially been observed in 2MASS ([Skrutskie et al., 2006](#); [Jao et al., 2018](#)); however, the significance of this detection is quite weak and it relies on the prior of the Gap's location from Gaia data. Further, the Gap is also present in Gaia Early Data Release 3 (EDR3)

([Jao & Feiden, 2021](#)). These EDR3 and 2MASS data sets then indicate that this feature is not a bias inherent to DR2.

The Gap is generally attributed to convective instabilities in the cores of stars straddling the fully convective transition mass (0.3 - 0.35 M<sub>⊙</sub>) ([Baraffe & Chabrier, 2018](#)). These instabilities interrupt the normal, slow, main sequence luminosity evolution of a star and result in luminosities lower than expected from the main sequence mass-luminosity relation ([Jao & Feiden, 2020](#)).

The Jao Gap, inherently a feature of M Dwarf populations, provides an enticing and unique view into the interior physics of these stars ([Feiden et al., 2021](#)). This is especially important as, unlike more massive stars, M Dwarf seismology is infeasible due to the short periods and extremely small magnitudes which both radial and low-order low-degree non-radial seismic waves are predicted to have in such low mass stars ([Rodríguez-López, 2019](#)). The Jao Gap therefore provides one of the only current methods to probe the interior physics of M Dwarfs.

The magnetic activity of M dwarfs is of particular interest due to the theorised links between habitability and the magnetic environment which a planet resides within. M dwarfs are known to be more magnetically active than earlier type stars while simultaneously this same high activity calls into question the canonical magnetic dynamo believed to drive the magnetic field of solar like stars (the  $\alpha\Omega$  dynamo). One primary challenge which M dwarfs pose is that stars less than approximately 0.35 M<sub>⊙</sub> are composed of a single convective region. This denies any dynamo model differential rotation between adjacent levels within the star. Alternative dynamo models have been proposed, such as the  $\alpha^2$  dynamo along with modifications to the  $\alpha\Omega$  dynamo which may be predictive of M dwarf magnetic fields.

Despite this work, very few studies have dived specifically into the magnetic field of M dwarfs at or near the convective transition region ([CITATION](#)). This is not surprising as that only spans approximately 0.2 mag in the Gaia BP-RP color magnitude diagram and is therefore populated by a relatively small number of stars.

([Jao et al., 2023](#)) identify the Jao gap as a strong discontinuity point for magnetic activity in M dwarfs. Two primary observations from their work are that the Gap

serves as a boundary where very few active stars in their sample of 640 M dwarfs exist below the gap and that the overall downward trend of activity moving to fainter magnitudes is anomalously high in within the 0.2 mag range of the gap. [Jao et al.](#) Figures 3 and 13 make this paucity in H $\alpha$  emission particularly clear. Based on previous work from [Spada & Lanzafam 2020](#), [Curtis et al. 2020](#), and [Dungee et al. 2022](#) the authors propose that the mechanism resulting in the reduced fraction of active stars within the gap is that as the radiative zone dissipates due to core expansion, angular momentum from the outer convective zone is dumped into the core resulting in a faster spin down than would otherwise be possible. Effectively the core of the star acts as a sink, reducing the amount of angular momentum which needs to be lost by magnetic braking for the outer convective region to reach the same angular velocity. Given that H $\alpha$  emission is strongly coupled magnetic activity in the lower photosphere and that a stars angular velocity is a primary factor in its magnetic activity, a faster spin down will serve to more quickly dampen H $\alpha$  activity.

In addition to H $\alpha$  the Calcium Fraunhauer lines may be used to trace the magnetic activity of a star. These lines originate from magnetic heating of the upper chromosphere driven by magnetic shear stresses within the star. [Boudreux et al. \(2022\)](#) and [Perdelwitz et al. \(2021\)](#) presented calcium emission measurements for stars spanning the Jao Gap. In this paper we search for similar trends in the Ca II H& K emission as [Jao et al.](#) see in the H $\alpha$  emission. In Section 11.2 we investigate the empirical star-to-star variability in emission and quantify if this could be due to noise or sample bias; in Section 11.3 we present a simplified toy model which shows that the mixing events characteristic of convective kissing instabilities could lead to increased star-to-star variability in activity as is seen empirically.

## 11.2 Correlation

Using Ca II H&K emission data from [Boudreux et al. \(2022\)](#) and [Perdelwitz et al. \(2021\)](#) (quantified using the  $R_{HK}$  metric) we investigate the correlation between the Jao Gap magnitude and stellar magnetic activity. We are more statistically limited here than past authors have been due to the requirement for high resolution

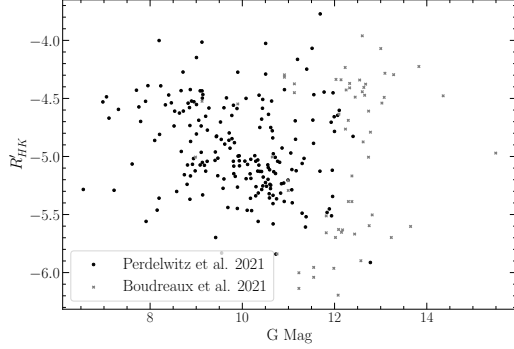


Figure 11.1: Merged Dataset from [Boudreault et al. \(2022\)](#); [Perdelwitz et al. \(2021\)](#). Note the increase in the spread of  $R'_{HK}$  around the Jao Gap Magnitude.

spectroscopic data when measuring Calcium emission; however, this is balanced by the apparent stronger correlation between Calcium emission and the Jao gap when compared to H $\alpha$  emission.

The merged dataset is presented in Figure 11.1. There is a visual discontinuity just below the Jao Gap magnitude; however, this manifests as an increase in the spread of the emission measurements rather than a change in the mean value. In order to quantify the significance of this discontinuity we measure the false alarm probability of the change in standard deviation.

First we split the merged dataset into bins with a width of 0.5 mag. In each bin we measure the standard deviation about the mean of the data. The results of this are shown in Figure 11.2. In order to measure the false alarm probability of this discontinuity we first resample the merged calcium emission data based on the associated uncertainties for each datum as presented in their respective publications. Then, for each of these “resample trials” we measure the probability that a change in the standard deviation of the size seen would happen purely due to noise. Results of this test are show in in Figure 11.3.

This rapid increase star-to-star variability would only arise due purely to noise  $0.3 \pm 0.08$  percent of the time and is therefore likely either a true effect or an alias of some sample bias. **COME BACK TO HERE TO FLUSH OUT SAMPLE BIAS SECTION.**

If the observed increase in variability is not due to a sample bias and rather is a

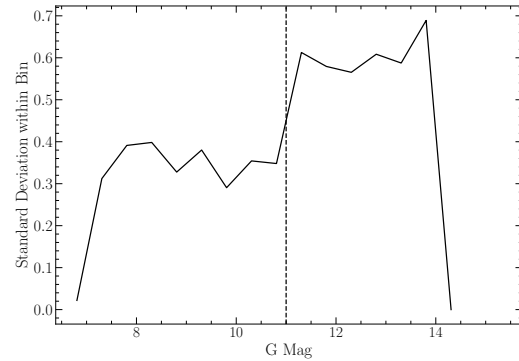


Figure 11.2: Standard deviation of Calcium emission data within each bin. Note the discontinuity near the Jao Gap Magnitude.

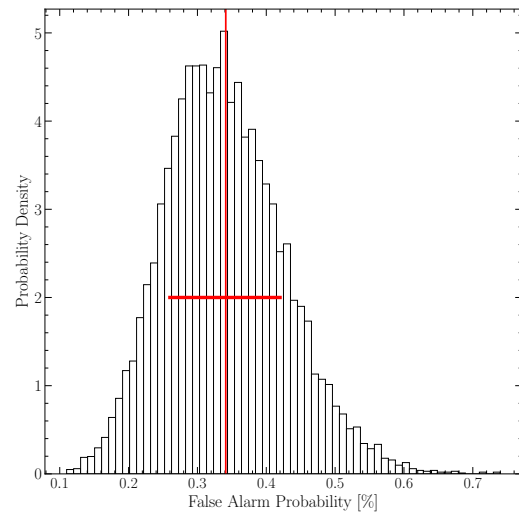


Figure 11.3: Probability distribution of the false alarm probability for the discontinuity seen in Figure 11.2. The mean of this distribution is  $0.341\% \pm 0.08$ .

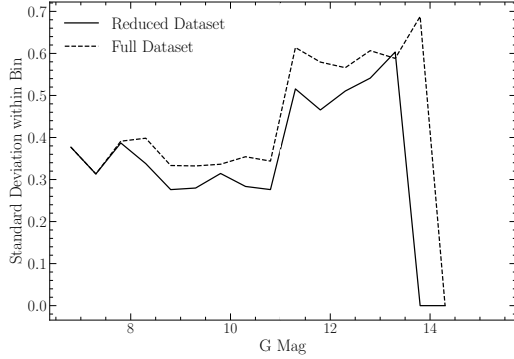


Figure 11.4: Spread in the magnetic activity metric for the merged sample with any stars  $\log(R'_{HK}) > -4.436$  filtered out.

physically driven effect then there is an obvious similarity between these findings and those of (Jao et al., 2023). Specifically we find a increase in variability just below the magnitude of the gap. Moreover, this variability increase is primarily driven by an increase in the number of low activity stars (as opposed to an increase in the number of high activity stars). We can further investigate the observed change in variability for only low activity stars by filtering out those stars at or above the saturated threshold for magnetic activity. Boudreault et al. (2022) identify  $\log(R'_{HK}) = -4.436$  as the saturation threshold. We adopt this value and filter out all stars where  $\log(R'_{HK}) \geq -4.436$ . Applying the same analysis to this reduced dataset as was done to the full dataset we still find a discontinuity at the same location (Figure 11.4). This discontinuity is of a smaller magnitude and consequently is more likely to be due purely to noise, with a  $7 \pm 0.2$  percent false alarm probability. This false alarm probability is however only concerned with the first point after the jump in variability. If we consider the false alarm probability of the entire high variability region then the probability that the high variability region is due purely to noise drops to  $1.4 \pm 0.04$  percent.

We observe a strong, likely statistically significant, discontinuity in the star-to-star variability of Ca II K & K emission just below the magnitude of the Jao Gap. However, modeling is required to determine if this discontinuity may be due to the same underlying physics.

While the observed increase in variability seen here does not seem to be coincident

with the Jao Gap — instead appearing to be approximately 0.5 mag fainter, in agreement with what is observed in [Jao et al. \(2023\)](#) — a number of complicating factors prevent us from falsifying that the these two features are not coincident. [Jao et al.](#) find, similar to the results presented here, that the paucity of  $H\alpha$  emission originates just below the gap. Moreover, we use a 0.5 magnitude bin size when measuring the star-to-star variability which injects error into the positioning of any feature in magnitude space. We can quantify the degree of uncertainty the magnitude bin choice injects by conducting Monte Carlo trials where bins are randomly shifted redder or bluer. We conduct 10,000 trials where each trial involves sampling a random shift to the bin start location from a normal distribution with a standard deviation of 1 magnitude. For each trial we identify the discontinuity location as the maximum value of the gradient of the standard deviation (effectively this is just the derivative of 11.4). Some trials result in the maximal value lying at the 0th index of the magnitude array due to edge effects, these trials are rejected (and account for 11% of the trials). The uncertainty in the identified magnitude of the discontinuity due to the selected start point of the magnitude bins reveals a  $1\sigma = \pm 0.32$  magnitude uncertainty in the location of the discontinuity (Figure 11.5). Finally, all previous studies of the M dwarf gap ([Jao et al., 2018](#); [?](#); [Mansfield & Kroupa, 2021](#); [Boudreux et al., 2022](#); [Jao et al., 2023](#)) demonstrate that the gap has a color dependency, shifting to fainter magnitudes as the population reddens and consequently an exact magnitude range is ill-defined. Therefore we cannot falsify the model that the discontinuity in star-to-star activity variability is coincident with the Jao Gap magnitude.

### 11.2.1 Rotation

Following the process described in [?](#), we first put the dataset through `stella` ([Feinstein et al., 2020b,a](#)), a convolutional neural network that trains a multitude of models, given a different initial seed, on TESS 2-min cadence. In this case, we also used an ensemble of 100 models to optimize the gains. `stella` identifies flares given a score of 0 to 1, here we use a score of 0.5 and above as flare identification. Furthermore, we also bin the data from a 2-min to 10-min cadence using `lightkurve`'s binning

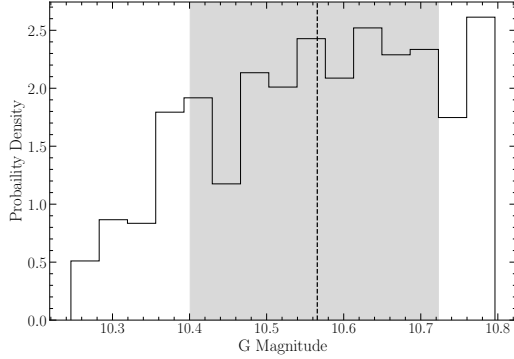


Figure 11.5: Probability density distribution of discontinuity location as identified in the merged dataset. The dashed line represents the mean of the distribution while the shaded region runs from the 16th percentile to the 84th percentile of the distribution. This distribution was built from 10,000 independent samples where the discontinuity was identified as the highest value in the gradient of the standard deviation.

function ([Lightkurve Collaboration et al., 2018](#); [Barentsen et al., 2020](#)). Not only does this help further reduce any flaring-contribution that might have been missed by `stella`<sup>1</sup>, but it also optimizes computational efficiency. Subsequently, we calculate residuals by subtracting the model from the data, retaining data with residuals smaller than 4 times the root-mean-square.

As M dwarfs often exhibit non-sinusoidal and quasi-periodic rotational variability, we employ Gaussian processes for modeling based on [Angus et al. \(2018\)](#) for the subset of M Dwarfs with no fiducial periods. The `starspot` package is adapted for light curve analysis ([Angus, 2021](#); ?) and accessible at (HAVEN'T DONE IT YET-AYLIN). Our Gaussian process kernel function incorporates two stochastically-driven simple harmonic oscillators, representing primary ( $P_{\text{rot}}$ ) and secondary ( $P_{\text{rot}}/2$ ) rotation modes. First, we implement the Lomb-Scargle periodogram within `starspot` to initially estimate the period. After which, we create a maximum a posteriori (MAP) fit using `starspot` to generate a model for stellar rotation. To obtain the posterior of the stellar rotation model, we use Markov Chain Monte Carlo (MCMC) sampling using the `pymc3` package (?) within our adapted `starspot` version.

ANALYSIS PART YET TO BE DETERMINED.

---

<sup>1</sup>This is relevant for flares that are misshapen at the start or break in the dataset due to missing either the ingress or egress.

### 11.2.2 Limitations

There are two primary limitation of our dataset. First, we only have 232 stars in our dataset limiting the statistical power of our analysis. This is primarily due to the relative difficulty of obtaining Ca II H&K measurements compared to obtaining  $H\alpha$  measurements. Reliable measurements require both high spectral resolutions ( $R \sim \text{XXXXXX}$ ) and a comparatively blue wavelength range <sup>2</sup>.

Additionally, the sample we do have does not extend to as low mass as would be ideal. This presents a degeneracy between two potential causes for the observed increased star-to-star variability. One option, as presented above and elaborated on in the following section, is that this is due to kissing instabilities. However, another possibility is that this increased variability is intrinsic to the magnetic fields of fully convective stars. There is limited discussion in the literature of the latter effect; however, Shulyak et al. (2019) present estimated magnetic field strengths for 47 M dwarfs, spanning a larger area around the convective transition region and their dataset does not indicate a inherently increased variability for fully convective stars (fully confirm this, not just visually).

## 11.3 Modeling

One of the most pressing questions related to this work is whether or not the increased star-to-star variability in the activity metric and the Jao Gap, which are coincident in magnitude, are driven by the same underlying mechanism. The challenge when addressing this question arises from current computational limitations. Specifically, the kinds of three dimensional magneto-hydrodynamical simulations — which would be needed to derive the effects of convective kissing instabilities on the magnetic field of the star — are infeasible to run over gigayear timescales while maintaining thermal timescale resolutions needed to resolve periodic mixing events.

In order to address this and answer the specific question of *could kissing instabilities result in increased star-to-star variability of the magnetic field*, we adopt a very

---

<sup>2</sup>wrt. too what many spectrographs cover. There is no unified resource listing currently commissioned spectrographs; however, it is somewhat hard to source glass which transmits well at H&K wavelengths limiting the lower wavelength of most spectrographs.

simple toy model. Kissing instabilities result in transient radiative zone separating the core of a star (convective) from its envelope (convective). When this radiative zone breaks down two important things happen: one, the entire star becomes mechanically coupled, and two, convective currents can now move over the entire radius of the star. [Jao et al. \(2023\)](#) propose that this mechanical coupling may allow the stars core to act as an angular momentum sink thus accelerating a stars spin down and resulting in anomalously low H $\alpha$  emission.

Regardless of the exact mechanism by which the magnetic field may be effected, it is reasonable to expect that both the mechanical coupling and the change to the scale of convective currents will have some effect on the stars magnetic field. On a microscopic scale both of these will change how packets of charge within a star move and may serve to disrupt a stable dynamo. Therefore, in the model we present here we make only one primary assumption: *every mixing event may modify the stars magnetic field by some amount*. Within our model this assumption manifests as a random linear perturbation applied to some base magnetic field at every mixing event. The strength of this perturbation is sampled from a normal distribution with some standard deviation,  $\sigma_B$ .

Synthetic stars are sampled from a grid of stellar models evolved using the Dartmouth Stellar Evolution Program (DSEP). Each stellar model was evolved using a high temporal resolution (timesteps no larger than 10,000 years [Check this](#)) and typical numerical tolerances of one part in  $10^5$ . Each model was based on a GS98 ([Grevesse & Sauval, 1998](#)) solar composition with a mass range from  $0.3 M_\odot$  to  $0.4 M_\odot$ . Finally, models adopt OPLIB high temperature radiative opacities, Ferguson 2004 low temperature radiative opacities, and include both atomic diffusion and gravitational settling. A Kippenhan-Iben diagram showing the structural evolution of a model within the gap is shown in Figure 11.6.

Each synthetic star is assigned some base magnetic activity ( $B_0 \sim \mathcal{N}(1, \sigma_B)$ ) and then the number of mixing events before some age  $t$  are counted based on local maxima in the core temperature. The toy magnetic activity at age  $t$  for the model is given in Equation 11.1. An example of the magnetic evolution resulting from this

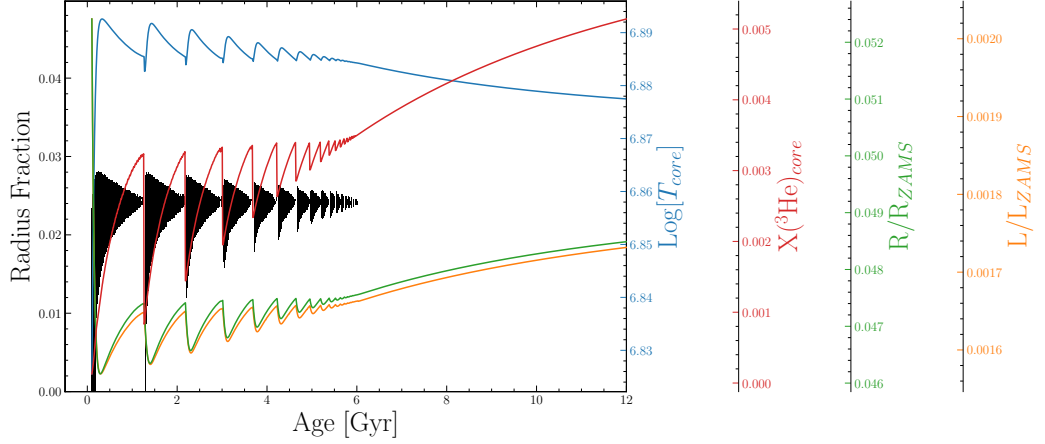


Figure 11.6: Kippenhan-Iben diagram for a 0.345 solar mass star. Note the periodic mixing events (where the plotted curves peak).

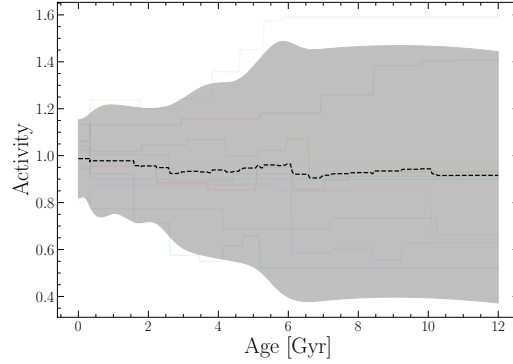


Figure 11.7: Example of the toy model presented here resulting in increased divergence between stars magnetic fields. The shaded region represents the maximum spread in the two point correlation function at each age.

model is given in Figure 11.7. Fundamentally, this model presents magnetic activity variation due to mixing events as a random walk and therefore results will increasingly diverge over time.

$$B(t) = B_0 + \sum_i B_i \sim \mathcal{N}(1, \sigma_B) \quad (11.1)$$

Applying the same analysis to these models as was done to the observations as described in Section X.X we find that this simple model results in a qualitatively similar trend in the standard deviation vs. Magnitude graph (Figure 11.8). In order

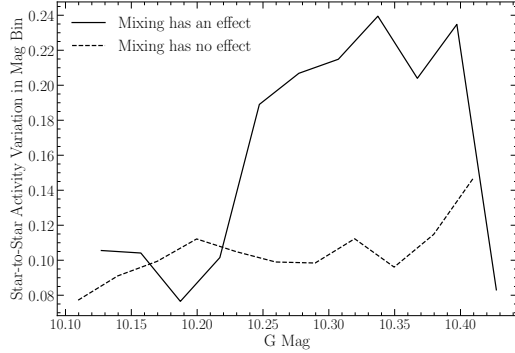


Figure 11.8: Toy model results showing a qualitatively similar discontinuity in the star-to-star magnetic activity variability.

to reproduce the approximately 50 percent change to the spread of the activity metric observed in the combined dataset in section 11.2 a distribution with a standard deviation of 0.1 is required when sampling the change in the magnetic activity metric at each mixing event. This corresponds to 68% of mixing events modifying the activity strength by 10 percent or less. The interpretation here is important, what this qualitative similarity demonstrates is that it may be reasonable to expect kissing instabilities to result in the observed increased star-to-star variation. Importantly, we are not able to claim that kissing instabilities *do* lead to these increased variations, only that they reasonably could. Further modeling, observational, and theoretical efforts will be needed to more definitively answer this question.

### 11.3.1 Limitations

The model presented in this paper is very limited and it is important to keep those limitations in mind when interpreting the results presented here. Some of the main challenges which should be leveled at this model are the assumption that the magnetic field will be altered by some small random perturbation at every mixing event. This assumption was informed by the large number of free parameters available to a physical star during the establishment of a large scale magnetic field and the associated likely stochastic nature of that process. However, it is similarly believable that the magnetic field will tend to alter in a uniform manner at each mixing event. For example, since differential rotation is generally proportional to the temperature

gradient within a star and activity is strongly coupled to differential rotation then it may be that as the radiative zone reforms over thermal timescales the homogenization of angular momentum throughout the star results in overall lower amounts of differential rotation each after mixing event than would otherwise be present.

Moreover, this model does not consider how other degenerate sources of magnetic evolution such as stellar spin down, relaxation, or coronal heating may effect star-to-star variability. These could conceivably lead to a similar increase in star-to-star variability which is coincident with the Jao Gap magnitude as the switch from fully to partially convective may effect efficiency of these process.

Additionally, there are challenges with this toy model that originate from the stellar evolutionary model. Observations of the Jao Gap show that the feature is not perpendicular to the magnitude axis; rather, it is inversely proportional to the color. No models of the Jao Gap published at the time of writing capture this color dependency and *what causes this color dependency* remains one of the most pressing questions relating to the underlying physics. This non captured physics is one potential explanation for why the magnitude where our model predicts the increase in variability is not in agreement with where the variability jump exists in the data.

Finally, we have not considered detailed descriptions of the dynamos of stars. The magnetohydrodynamical modeling which would be required to model the evolution of the magnetic field of these stars at thermal timescale resolutions over gigayears is currently beyond the ability of practical computing. Therefore future work should focus on limited modeling which may inform the evolution of the magnetic field directly around the time of a mixing event.

## 11.4 Conclusion

It is, at this point, well established that the Jao Gap may provide a unique view of the interiors of stars for which other probes, such as seismology, fail. However, it has only recently become clear that the Gap may lend insight into not just structural changes within a star but also into the magnetic environment of the star. [Jao et al. \(2023\)](#) presented evidence that the physics driving the Gap might additionally result

in a paucity of H $\alpha$  emission. These authors propose potential physical mechanisms which could explain this paucity, including the core of the star acting as an angular momentum sink during mixing events.

Here we have expanded upon this work by probing the degree and variability of Calcium II H&K emission around the Jao Gap. We lack the same statistical power of [Jao et al.](#)'s sample; however, by focusing on the star-to-star variability within magnitude bins we are able to retain statistical power. We find that there is an anomalous increase in variability at a G magnitude of  $\sim 11$ . This is only slightly below the observed mean gap magnitude.

Additionally, we propose a simple model to explain this variability. Making the assumption that the periodic convective mixing events will have some small but random effect on the overall magnetic field strength we are able to qualitatively reproduce the increase activity spread in a synthetic population of stars.

## **Part IV**

# **Conclusions**



# Bibliography

- Alcaino, G. 1975, A&AS, 21, 15
- Amard, L., Palacios, A., Charbonnel, C., et al. 2019, A&A, 631, A77
- Angus, R. 2021, Zenodo, doi:10.5281/zenodo.4613887
- Angus, R., Morton, T., Aigrain, S., Foreman-Mackey, D., & Rajpaul, V. 2018, Monthly Notices of the Royal Astronomical Society, 474, 2094
- Astropy Collaboration, Price-Whelan, A. M., Sipőcz, B. M., et al. 2018, AJ, 156, 123
- Astudillo-Defru, N., Delfosse, X., Bonfils, X., et al. 2017, A&A, 600, A13
- Bahcall, J. N., Pinsonneault, M. H., & Basu, S. 2001, ApJ, 555, 990
- Bahcall, J. N., Serenelli, A. M., & Basu, S. 2005, ApJL, 621, L85
- Baraffe, I., & Chabrier, G. 2018, A&A, 619, A177
- Baraffe, I., Chabrier, G., Allard, F., & Hauschildt, P. H. 1997, A&A, 327, 1054
- Barber, C. B., Dobkin, D. P., & Huhdanpaa, H. 1996, ACM Transactions on Mathematical Software (TOMS), 22, 469
- Barentsen, G., Hedges, C., Vinícius, Z., et al. 2020, KeplerGO/Lightkurve: Lightkurve v1.11.0, Zenodo, , , doi:10.5281/zenodo.3836658
- Barnes, J., Cameron, A. C., Donati, J.-F., et al. 2005, Monthly Notices of the Royal Astronomical Society: Letters, 357, L1
- Barnes, J., James, D., & Cameron, A. C. 2004, Monthly Notices of the Royal Astronomical Society, 352, 589

- Baroch, D., Morales, J. C., Ribas, I., et al. 2020, A&A, 641, A69
- Bastian, N., & Lardo, C. 2015, MNRAS, 453, 357
- Bastian, N., & Lardo, C. 2018, Annual Review of Astronomy and Astrophysics, 56, 83
- Baumgardt, H., & Makino, J. 2003, MNRAS, 340, 227
- Bekki, K., & Chiba, M. 2002, The Astrophysical Journal, 566, 245. <https://dx.doi.org/10.1086/337984>
- Bernstein, R., Shectman, S. A., Gunnels, S. M., Mochnacki, S., & Athey, A. E. 2003, in Society of Photo-Optical Instrumentation Engineers (SPIE) Conference Series, Vol. 4841, Proc. SPIE, ed. M. Iye & A. F. M. Moorwood, 1694–1704
- Berta, Z. K., Irwin, J., Charbonneau, D., Burke, C. J., & Falco, E. E. 2012, AJ, 144, 145
- Bjork, S. R., & Chaboyer, B. 2006, ApJ, 641, 1102
- Boudreaux, E. M., Newton, E. R., Mondrik, N., Charbonneau, D., & Irwin, J. 2022, ApJ, 929, 80
- Boylan-Kolchin, M. 2018, MNRAS, 1423
- Brodie, J. P., & Strader, J. 2006, Annu. Rev. Astron. Astrophys., 44, 193
- Brown, J. H., Burkert, A., & Truran, J. W. 1991, ApJ, 376, 115  
—. 1995, ApJ, 440, 666
- Browning, M. K., Basri, G., Marcy, G. W., West, A. A., & Zhang, J. 2010, AJ, 139, 504
- Cameron, R. H., Dikpati, M., & Brandenburg, A. 2017, Space Science Reviews, 210, 367. <https://doi.org/10.1007/s11214-015-0230-3>
- Carretta, E. 2013, A&A, 557, A128

- Carretta, E., Bragaglia, A., Gratton, R. G., et al. 2010, *Astronomy & Astrophysics*, 516, A55
- Catalano, S., & Marilli, E. 1983, *A&A*, 121, 190
- Chaboyer, B., Fenton, W. H., Nelan, J. E., Patnaude, D. J., & Simon, F. E. 2001, *ApJ*, 562, 521
- Chabrier, G., & Baraffe, I. 1997, *A&A*, 327, 1039
- Charbonneau, P. 2014, *ARA&A*, 52, 251
- Choi, J., Dotter, A., Conroy, C., et al. 2016, *ApJ*, 823, 102
- Colgan, J., Kilcrease, D. P., Magee, N. H., et al. 2016, in *APS Meeting Abstracts*, Vol. 2016, APS Division of Atomic, Molecular and Optical Physics Meeting Abstracts, D1.008
- Cowling, T. G. 1966, *QJRAS*, 7, 121
- Creevey, O. L., Sordo, R., Pailler, F., et al. 2022, arXiv e-prints, arXiv:2206.05864
- de Mink, S. E., Pols, O. R., Langer, N., & Izzard, R. G. 2009, *A&A*, 507, L1
- Decressin, T., Meynet, G., Charbonnel, C., Prantzos, N., & Ekström, S. 2007, *A&A*, 464, 1029
- Delfosse, X., Forveille, T., Perrier, C., & Mayor, M. 1998, *A&A*, 331, 581
- Denissenkov, P. A., & Hartwick, F. D. A. 2014, *MNRAS*, 437, L21
- D'Ercole, A., D'Antona, F., Ventura, P., Vesperini, E., & McMillan, S. L. W. 2010, *MNRAS*, 407, 854
- D'Ercole, A., Vesperini, E., D'Antona, F., McMillan, S. L. W., & Recchi, S. 2008, *MNRAS*, 391, 825
- DIERCKX, P. 1981, *IMA Journal of Numerical Analysis*, 1, 267. <https://doi.org/10.1093/imamanum/1.3.267>
- Dikpati, M., & Charbonneau, P. 1999, *ApJ*, 518, 508

- Dotter, A. 2016, ApJS, 222, 8
- Dotter, A., Chaboyer, B., Jevremović, D., et al. 2008, The Astrophysical Journal Supplement Series, 178, 89
- Dotter, A., Ferguson, J. W., Conroy, C., et al. 2015, MNRAS, 446, 1641
- Earl, N., Tollerud, E., Jones, C., et al. 2021, astropy/specutils: v1.3, vv1.3, Zenodo, doi:10.5281/zenodo.4987675. <https://doi.org/10.5281/zenodo.4987675>
- Emden, R. 1907, Gaskugeln
- Feiden, G. A., Skidmore, K., & Jao, W.-C. 2021, ApJ, 907, 53
- Feinstein, A., Montet, B., & Ansdell, M. 2020a, J. Open Source Softw., 5, 2347
- Feinstein, A. D., Montet, B. T., Ansdell, M., et al. 2020b, Astron. J., 160, 219
- Ferguson, J. W., Alexander, D. R., Allard, F., et al. 2005, ApJ, 623, 585
- Ferguson, T. S. 1973, The annals of statistics, 209
- Fontes, C. J., Zhang, H. L., Abdallah, J., J., et al. 2015, Journal of Physics B Atomic Molecular Physics, 48, 144014
- Gaia Collaboration, Smart, R. L., Sarro, L. M., et al. 2021, A&A, 649, A6
- Gastine, T., Yadav, R. K., Morin, J., Reiners, A., & Wicht, J. 2014, MNRAS, 438, L76
- Gratton, R., Sneden, C., & Carretta, E. 2004, ARA&A, 42, 385
- Gratton, R. G., Carretta, E., & Bragaglia, A. 2012, Astronomy and Astrophysics Reviews, 20, 50
- Grevesse, N., Asplund, M., & Sauval, A. J. 2007, SSRv, 130, 105
- Grevesse, N., & Sauval, A. J. 1998, SSRv, 85, 161
- Gustafsson, B., Edvardsson, B., Eriksson, K., et al. 2008, A&A, 486, 951
- Hakel, P., Sherrill, M. E., Mazevet, S., et al. 2006, JQSRT, 99, 265

- Hall, J. C., Lockwood, G. W., & Skiff, B. A. 2007, *The Astronomical Journal*, 133, 862. <https://doi.org/10.1086%2F510356>
- Hawley, S. L., Gizis, J. E., & Reid, I. N. 1996, *AJ*, 112, 2799
- Hawley, S. L., & Pettersen, B. R. 1991, *ApJ*, 378, 725
- Henyey, L. G., Forbes, J. E., & Gould, N. L. 1964, *ApJ*, 139, 306
- Houdebine, E. R., Mullan, D. J., Bercu, B., Paletou, F., & Gebran, M. 2017, *ApJ*, 837, 96
- Hudson, M. J., & Robison, B. 2018, *Monthly Notices of the Royal Astronomical Society*, 477, 3869
- Husser, T. O., Wende-von Berg, S., Dreizler, S., et al. 2013, *A&A*, 553, A6
- Iglesias, C. A., & Rogers, F. J. 1996, *ApJ*, 464, 943
- Irwin, J., Berta, Z. K., Burke, C. J., et al. 2011, *ApJ*, 727, 56
- Jao, W.-C., & Feiden, G. A. 2020, *AJ*, 160, 102
- . 2021, *Research Notes of the American Astronomical Society*, 5, 124
- Jao, W.-C., Henry, T. J., Gies, D. R., & Hambly, N. C. 2018, *ApJL*, 861, L11
- Jao, W.-C., Henry, T. J., White, R. J., et al. 2023, *AJ*, 166, 63
- Jermyn, A. S., Bauer, E. B., Schwab, J., et al. 2022, arXiv e-prints, arXiv:2208.03651
- Jordán, A., Côté, P., West, M. J., & Marzke, R. O. 2002, *ApJL*, 576, L113
- Joyce, M., & Chaboyer, B. 2018, *ApJ*, 864, 99
- Kelson, D. D. 2003, *PASP*, 115, 688
- Kelson, D. D., Illingworth, G. D., van Dokkum, P. G., & Franx, M. 2000, *ApJ*, 531, 159
- Kesseli, A. Y., Muirhead, P. S., Mann, A. W., & Mace, G. 2018, *AJ*, 155, 225

- Kostogryz, N., Shapiro, A. I., Witzke, V., et al. 2023, Research Notes of the AAS, 7, 39. <https://dx.doi.org/10.3847/2515-5172/acc180>
- Kovetz, A., Yaron, O., & Prialnik, D. 2009, MNRAS, 395, 1857
- Kravtsov, A. V., & Gnedin, O. Y. 2005, The Astrophysical Journal, 623, 650
- Kurucz, R.-L. 1993, Kurucz CD-Rom, 13
- Latour, M., Husser, T. O., Giesers, B., et al. 2019, A&A, 631, A14
- Lehtinen, J. J., Käpylä, M. J., Olspert, N., & Spada, F. 2020, arXiv e-prints, arXiv:2007.00040
- Lightkurve Collaboration, Cardoso, J. V. d. M., Hedges, C., et al. 2018, Astrophysics Source Code Library, ascl:1812.013
- Lovis, C., Ségransan, D., Mayor, M., et al. 2011, Astronomy & Astrophysics, 528, A112
- MacDonald, J., & Gizis, J. 2018, MNRAS, 480, 1711
- Magaudda, E., Stelzer, B., Covey, K. R., et al. 2020, A&A, 638, A20
- Magee, N. H., Abdallah, J., Colgan, J., et al. 2004, in American Institute of Physics Conference Series, Vol. 730, Atomic Processes in Plasmas: 14th APS Topical Conference on Atomic Processes in Plasmas, ed. J. S. Cohen, D. P. Kilcrease, & S. Mazzavent, 168–179
- Mamajek, E. E., & Hillenbrand, L. A. 2008, ApJ, 687, 1264
- Mann, A. W., Gaidos, E., Mace, G. N., et al. 2016, ApJ, 818, 46
- Mansfield, S., & Kroupa, P. 2021, A&A, 650, A184
- Marigo, P., & Aringer, B. 2009, A&A, 508, 1539
- Marigo, P., Aringer, B., Girardi, L., & Bressan, A. 2022, ApJ, 940, 129
- Marino, A. F., Milone, A. P., Karakas, A. I., et al. 2015, Monthly Notices of the Royal Astronomical Society, 450, 815. <https://doi.org/10.1093/mnras/stv420>

- Medina, A. A., Winters, J. G., Irwin, J. M., & Charbonneau, D. 2020, ApJ, 905, 107
- Middelkoop, F. 1982, A&A, 107, 31
- Milone, A. P., Piotto, G., Bedin, L. R., et al. 2012, ApJ, 744, 58
- Milone, A. P., Marino, A. F., Piotto, G., et al. 2015a, ApJ, 808, 51
- . 2015b, MNRAS, 447, 927
- Milone, A. P., Piotto, G., Renzini, A., et al. 2017, MNRAS, 464, 3636
- Milone, A. P., Marino, A. F., Renzini, A., et al. 2018, MNRAS, 481, 5098
- Newton, E. R., Irwin, J., Charbonneau, D., et al. 2017, The Astrophysical Journal, 834, 85
- Newton, E. R., Irwin, J., Charbonneau, D., et al. 2016, ApJ, 821, 93
- Newton, E. R., Mondrik, N., Irwin, J., Winters, J. G., & Charbonneau, D. 2018, AJ, 156, 217
- Noyes, R. W., Hartmann, L. W., Baliunas, S. L., Duncan, D. K., & Vaughan, A. H. 1984, ApJ, 279, 763
- Núñez, A., Agüeros, M. A., Covey, K. R., et al. 2015, ApJ, 809, 161
- Nutzman, P., & Charbonneau, D. 2008, PASP, 120, 317
- Owen, J. E., & Mohanty, S. 2016, MNRAS, 459, 4088
- Pallavicini, R., Golub, L., Rosner, R., et al. 1981, ApJ, 248, 279
- Parker, E. N. 1955, ApJ, 122, 293
- . 1975, ApJ, 198, 205
- Paxton, B., Bildsten, L., Dotter, A., et al. 2011, The Astrophysical Journal Supplement Series, 192, 3
- Pedregosa, F., Varoquaux, G., Gramfort, A., et al. 2011, Journal of Machine Learning Research, 12, 2825

- Peebles, P. J. E., & Dicke, R. H. 1968, ApJ, 154, 891
- Peng, E. W., Ferguson, H. C., Goudfrooij, P., et al. 2011, The Astrophysical Journal, 730, 23
- Perdelwitz, V., Mittag, M., Tal-Or, L., et al. 2021, A&A, 652, A116
- Piotto, G., Bedin, L. R., Anderson, J., et al. 2007, The Astrophysical Journal Letters, 661, L53
- Piotto, G., Milone, A. P., Bedin, L. R., et al. 2015, AJ, 149, 91
- Pizzolato, N., Maggio, A., Micela, G., et al. 2000, in Astronomical Society of the Pacific Conference Series, Vol. 198, Stellar Clusters and Associations: Convection, Rotation, and Dynamos, ed. R. Pallavicini, G. Micela, & S. Sciortino, 71
- Plez, B. 2008, Physica Scripta Volume T, 133, 014003
- Prantzos, N., Charbonnel, C., & Iliadis, C. 2007, A&A, 470, 179
- Rauscher, E., & Marcy, G. W. 2006, PASP, 118, 617
- Reiners, A., Schüssler, M., & Passegger, V. M. 2014, ApJ, 794, 144
- Renzini, A. 2008, Monthly Notices of the Royal Astronomical Society, 391, 354.  
<https://doi.org/10.1111/j.1365-2966.2008.13892.x>
- Richer, H. B., Fahlman, G. G., Buonanno, R., et al. 1991, ApJ, 381, 147
- Robertson, P., Mahadevan, S., Endl, M., & Roy, A. 2014, Science, 345, 440
- Rodríguez-López, C. 2019, Frontiers in Astronomy and Space Sciences, 6, 76
- Rousseeuw, P. J. 1987, Journal of Computational and Applied Mathematics, 20, 53.  
<https://www.sciencedirect.com/science/article/pii/0377042787901257>
- Rutten, R. G. M. 1984, A&A, 130, 353
- Salaris, M., & Cassisi, S. 2005, Evolution of stars and stellar populations (John Wiley & Sons)

- Salvatier, J., Wiecki, T. V., & Fonnesbeck, C. 2016, PeerJ Computer Science, 2, e55.  
<https://doi.org/10.7717/peerj-cs.55>
- Sandage, A. R. 1953, AJ, 58, 61
- Sbordone, L., Salaris, M., Weiss, A., & Cassisi, S. 2011, Astronomy & Astrophysics, 534, A9
- Schmidt, S. J., Prieto, J. L., Stanek, K. Z., et al. 2014, ApJL, 781, L24
- Schrijver, C. J., & Rutten, R. G. M. 1987, A&A, 177, 143
- Schröder, C., Reiners, A., & Schmitt, J. H. M. M. 2009, A&A, 493, 1099
- Seaton, M. J., Yan, Y., Mihalas, D., & Pradhan, A. K. 1994, MNRAS, 266, 805
- Shields, A. L., Ballard, S., & Johnson, J. A. 2016, PhR, 663, 1
- Shulyak, D., Reiners, A., Nagel, E., et al. 2019, A&A, 626, A86
- Skrutskie, M. F., Cutri, R. M., Stiening, R., et al. 2006, AJ, 131, 1163
- Skumanich, A. 1972, ApJ, 171, 565
- Smith, G. H. 1987, Publications of the Astronomical Society of the Pacific, 99, 67.  
<https://dx.doi.org/10.1086/131958>
- Sneden, C., Kraft, R. P., Prosser, C. F., & Langer, G. 1992, The Astronomical Journal, 104, 2121
- Sollima, A. 2019, Monthly Notices of the Royal Astronomical Society, 489, 2377.  
<https://doi.org/10.1093/mnras/stz2093>
- Suárez Mascareño, A., Rebolo, R., & González Hernández, J. I. 2016, A&A, 595, A12
- Suárez Mascareño, A., Rebolo, R., González Hernández, J. I., & Esposito, M. 2015, MNRAS, 452, 2745
- Suntzeff, N. B., & Kraft, R. P. 1996, AJ, 111, 1913
- Thompson, M. J., Toomre, J., Anderson, E. R., et al. 1996, Science, 272, 1300

- Tomczyk, S., Schou, J., & Thompson, M. J. 1996, in American Astronomical Society Meeting Abstracts, Vol. 188, American Astronomical Society Meeting Abstracts #188, 69.03
- Torres, C. A. O., Quast, G. R., da Silva, L., et al. 2006, *A&A*, 460, 695
- Trampedach, R., Stein, R. F., Christensen-Dalsgaard, J., Nordlund, Å., & Asplund, M. 2014, *MNRAS*, 445, 4366
- Valle, G., Dell’Omodarme, M., & Tognelli, E. 2022, *A&A*, 658, A141
- van den Bergh, S. 2010, *The Astronomical Journal*, 140, 1043. <https://dx.doi.org/10.1088/0004-6256/140/4/1043>
- van Saders, J. L., & Pinsonneault, M. H. 2012, *ApJ*, 751, 98
- Vanderburg, A., Plavchan, P., Johnson, J. A., et al. 2016, *Monthly Notices of the Royal Astronomical Society*, 459, 3565
- Vaughan, A. H., Baliunas, S. L., Middelkoop, F., et al. 1981, *ApJ*, 250, 276
- Vaughan, A. H., & Preston, G. W. 1980, *Publications of the Astronomical Society of the Pacific*, 92, 385
- Ventura, P., & D’Antona, F. 2009, *A&A*, 499, 835
- Ventura, P., D’Antona, F., Mazzitelli, I., & Gratton, R. 2001, *ApJL*, 550, L65
- Vilhu, O. 1984, *A&A*, 133, 117
- West, A. A., Weisenburger, K. L., Irwin, J., et al. 2015, *ApJ*, 812, 3
- Wilson, O. C. 1963, *ApJ*, 138, 832
- . 1968, *ApJ*, 153, 221
- Wright, N. J., Drake, J. J., Mamajek, E. E., & Henry, G. W. 2011, *The Astrophysical Journal*, 743, 48. <https://doi.org/10.1088/0004-637x/743/2/f1>
- Wright, N. J., Newton, E. R., Williams, P. K. G., Drake, J. J., & Yadav, R. K. 2018, *MNRAS*, 479, 2351